Synthesis and Photoelectrochemical Characterization of (Ammonolyzed) Nb_2O_5 Thin Films

Master Thesis Dissertation by Mario Alonso

2798035

TU Darmstadt

Materials Science – Materials and Resources

Supervisors: Prof. Dr. Anke Weidenkaff

Abstract

Growing energy demand and the need to reduce CO_2 emissions have driven research into solar energy conversion technologies, such as water splitting by photoelectrochemical processes (PEC). In this context, niobium pentoxide (Nb_2O_5) is a promising material due to its stability and semiconducting properties, although its wide bandgap limits its absorption in the visible spectrum. To improve its performance, ammonolysis has been explored as a method to modify its electronic structure and enhance its photoelectrochemical response.

Nb_2O_5 thin films were synthesized by dip-coating on silicon and quartz glass substrates, followed by heat treatment and ammonolysis at temperatures of 750 and 800 °C in an ammonia atmosphere. Structural characterization confirmed the formation of Nb_2O_5 with a pseudohexagonal structure, while X-ray photoelectron spectroscopy (XPS) analysis demonstrated the incorporation of nitrogen in the ammonia-treated samples.

The performance of the photoelectrodes was evaluated through PEC tests under UV (500 W/m²) and visible (1000 W/m²) light illumination. On silicon substrates, films ammonolyzed at 800 °C showed a significant increase in photogenerated current under UV irradiation (~1 mA), indicating an improvement in charge separation efficiency. However, the response in the visible spectrum remained low (~100 μA), suggesting that although ammonolysis slightly reduces the bandgap, absorption is still insufficient for efficient visible light conversion. In contrast, films on quartz glass exhibited negligible photoelectrochemical activity, indicating that this substrate does not favor charge transport under the evaluated conditions.

Post-PEC XPS analysis revealed that the ammonolyzed samples suffered from charging effects, indicating a loss of conductivity. The survey spectrum showed an increase in oxygen and carbon content, likely due to contamination from the electrolyte or reaction intermediates. Additionally, the emergence of more pronounced silicon peaks suggests degradation or partial detachment of the thin film during electrochemical testing. The chemical stability evaluation was hindered by these charging effects, preventing a conclusive assessment of post-PEC oxidation states and composition.

In conclusion, ammonolysis at 800 °C enhances the PEC activity of Nb_2O_5 in the UV range but does not significantly improve its efficiency in the visible spectrum. Furthermore, the post-PEC analysis indicates that the thin films may degrade or detach over time under electrochemical conditions. These findings highlight the need for additional strategies, such as doping, heterostructure formation, or improved stabilization techniques, to optimize the material for long-term PEC applications.

1 Table of contents

2 List of Figures

3 List of Tables

4 Introduction

One of the main challenges facing humanity in the twenty-first century is to supply the world's population with sufficient energy to meet desired living standards. The power consumption of the current (2025) global population of approximately 8 billion people is estimated at around 18 TW, and these numbers are projected to increase to ~9.7 billion people and 30–35 TW by 2050.[1]

Fossil fuels, which currently provide about 80% of our energy supply, will struggle to keep up with this rising demand. In the long run, this is a matter of finite reserves. Based on current consumption rates, estimated reserves range from 120 to 300 years for coal, 40–70 years for oil, and 50–150 years for natural gas. However, the effects of dwindling reserves will be felt on a much shorter time scale, as extraction becomes increasingly difficult, and peak production is expected to occur long before supplies are fully depleted.[1]

A potentially far more serious issue related to the use of fossil fuels is their environmental impact. The primary concern is the emission of greenhouse gases, particularly CO_2, and their significant contribution to global warming.

The increasing demand for energy in recent decades has also led to a rise in anthropogenic activities, resulting in a greater reliance on fossil fuels. Consequently, CO_2 emissions have surged, driving atmospheric concentrations of this greenhouse gas from 340 ppm in 1980 (as recorded by NOAA's Mauna Loa Observatory) to 425 ppm in January 2025, as illustrated in Figure 1.

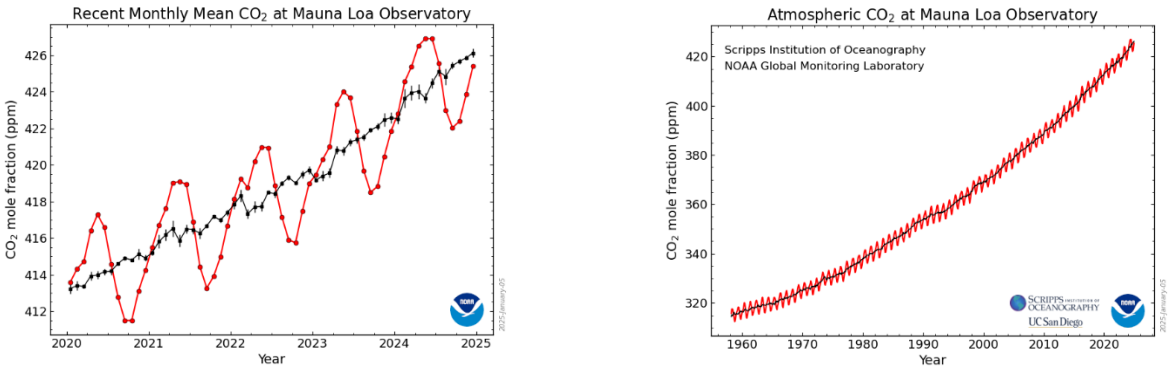

Figure 1: On the left, concentration of CO_2 in the atmosphere in recent years measured at NOAA`S Mauna Loa Observatory (Hawaii). On the right, concentration of $CO_2$ in the atmosphere in recent decades measured at NOAA`S Mauna Loa Observatory (Hawaii).[2]

This sharp increase in CO_2 levels has triggered severe environmental consequences, including rising sea levels, prolonged droughts, and more pronounced fluctuations in river flows, alongside a global rise in temperatures.[3]

To mitigate this negative effect, various national and international agreements have been established in recent years with the primary goal of reducing CO_2 emissions. The most significant international agreement in terms of emission reductions is the Paris Agreement (2015), which aims to prevent a global temperature increase of 2 °C (ideally 1.5 ºC).

Other ongoing initiatives to combat climate change include the European Green Deal, which aims to achieve climate neutrality through a green transition by 2050 (European Green Deal - Consilium), and the United Nations' Glasgow Climate Pact, which builds on the objectives proposed in the Paris Agreement (Climate Action - UN, 2021).[4]

Even though fossil fuels are expected to remain the primary energy source for many years, particularly for electricity generation and as fuel for vehicles, their gradual replacement with zero-CO_2-emission renewable energy sources is imperative to achieve the goals established in the aforementioned agreements.

4.1 Solar Water Splitting

One of the renewable energy sources gaining prominence today is hydrogen. Hydrogen can be obtained through various methods, including steam methane reforming (SMR), electrolysis, and solar water splitting. Currently, SMR is the most widely used method, but it relies on fossil fuels and emits CO_2. In contrast, electrolysis and solar water splitting utilize renewable energy sources to produce hydrogen with little to no emissions. The process of obtaining hydrogen through solar water splitting is based on utilizing solar energy to divide water molecules into their fundamental components: hydrogen (H_2) and oxygen (O_2). This process makes use of semiconductor materials that act as photocatalysts to capture light energy and convert it into chemical energy.[5]

Solar water splitting, a growing method for harnessing solar energy, stands as a promising technology for producing clean and sustainable fuels. As sunlight is an abundant and virtually inexhaustible energy source, available in most regions of the planet, solar water splitting aligns with the global push toward decarbonizing energy systems and reducing greenhouse gas emissions. Arguably, light is an even more available resource than water, so second-generation photovoltaic technologies would be more suitable, however, places with higher solar radiation are more inaccessible, as these areas are mostly deserts. Its renewability stems from the fact that solar radiation is naturally replenished daily, making it a sustainable alternative to fossil fuels.[6–8]

The concept of photocatalytic water splitting dates to the influential work of Fujishima and Honda in 1972, where TiO_2 was used as a photoanode to achieve water electrolysis under ultraviolet (UV) light. This breakthrough laid the foundation for exploring various semiconductor materials with tailored bandgap

properties, aimed at improving light absorption and facilitating the redox reactions necessary for hydrogen and oxygen generation.[7,8]

Solar water splitting involves two critical half-reactions: the oxidation of water (1) and the reduction of protons to hydrogen (2). For these reactions to occur, the conduction band of the photocatalyst must be sufficiently negative for hydrogen reduction, while the valence band must be positive enough for oxygen evolution. This energy alignment ensures that photogenerated electrons and holes can drive the respective redox reactions.

$$H_2O \rightarrow \frac{1}{2}O_2 + 2H^+ + 2\,e^- \quad (1)$$

$$2\,H^+ + 2\,e^- \rightarrow H_2 \quad (2)$$

As illustrated in Figure 2, a minimum bandgap of 1.23 eV is required; however, kinetic overpotentials often necessitate bandgaps closer to 2 eV for effective single-material systems.

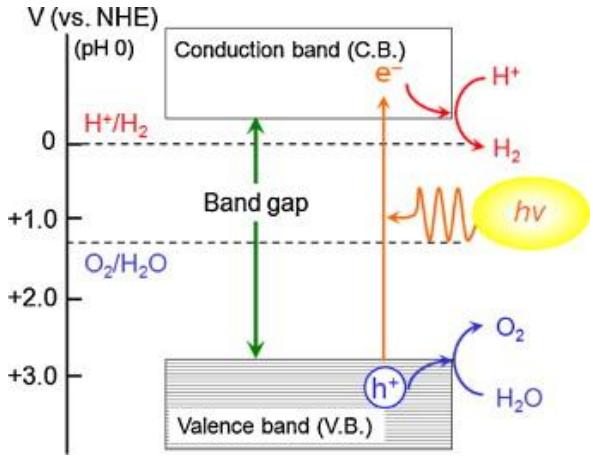

Figure 2: Basic principle of overall water splitting on a semiconductor particle.[9]

However, achieving efficient light absorption across the visible spectrum remains a major challenge. While wide-bandgap semiconductors like TiO_2 and ZnO offer high stability, their UV light activation limits their efficiency since UV accounts for only ~5% of the solar spectrum. To overcome this limitation, research has focused on narrow-bandgap materials, doped semiconductors, and heterojunction systems that enhance visible light absorption and charge carrier separation.[7,10]

Recent efforts have included the development of multi-junction photoelectrochemical (PEC) systems and photocatalysts. Tandem designs combining semiconductors with different bandgaps have achieved solar-to-hydrogen (STH) efficiencies exceeding 12% in laboratory settings. [7] Nanostructured materials and doping strategies have further improved charge mobility and reduced recombination losses. Examples include the

integration of noble metal co-catalysts like Pt and RuO_2 to enhance hydrogen evolution, though their high costs remain a barrier to scalability.[8]

4.2 Photoelectrocatalysis

Photoelectrochemical (PEC) water splitting is a specific approach within the broader category of solar water splitting (SWS), which also includes photocatalytic (PC) SWS and photovoltaic-driven (PV) SWS. In PEC SWS, sunlight is used to drive the production of hydrogen and oxygen from water through a photoelectrode system, where semiconductor materials with suitable bandgaps facilitate the required redox reactions. This process showcases the potential of PEC systems to convert solar energy into chemical energy efficiently. As a clean and sustainable energy solution, PEC SWS highlights the broader promise of solar-driven hydrogen production for addressing global energy challenges.[11]

Among the different solar water splitting (SWS) approaches, photoelectrochemical (PEC) water splitting stands out for its ability to directly integrate light absorption and electrochemical reactions within a single system. By leveraging photocatalysis (where light excites a semiconductor, generating electron-hole pairs) and electrocatalysis, which applies an electrical potential to enhance reaction efficiency, PEC systems offer a synergistic pathway for sustainable hydrogen production. On the other hand, photovoltaic technologies lose efficiency when heated, but the water in the PEC minimizes the stress by cooling the semiconductor while the heat helps the SWS. This dual mechanism not only optimizes solar-to-hydrogen conversion but also presents broader opportunities for environmental remediation and renewable energy applications. [12–14]

At its core, photoelectrocatalysis involves semiconductor materials capable of absorbing sunlight to generate excited charge carriers (electrons and holes). The energy required to excite an electron from the valence band (VB) to the conduction band (CB) of a semiconductor is defined by the bandgap (E_g), which must match the energy of the incident photons (3).

$$E_g = h\nu = \frac{hc}{\lambda} \tag{3}$$

Where h is Planck's constant (J/s), ν is the frequency of light (s^{-1}), c is the speed of light (m/s) and λ is the wavelength of the absorbed light (m).

For a material to be effective in photoelectrocatalysis, its bandgap must not only be adequate to absorb visible or near-visible light but also its band edges must align with the redox potentials of the desired reactions (equations 1 and 2).[13,14]

Advances in material science have driven the development of nanostructured photoelectrocatalysts, including metal oxides, metal-organic frameworks (MOFs), and hybrid materials. These innovations enhance light absorption, charge separation, and catalytic activity, making photoelectrocatalysis a viable option for renewable energy and environmental applications. For instance, materials such as titanium dioxide (TiO_2) and hematite (Fe_2O_3, which seems to be a good option, but it is not because of the polaronic state close to CEM prohibiting)[15] have shown promise for solar water splitting in the visible light range. Additionally, molecular catalysts, often based on transition metal complexes or organic frameworks, offer tunable electronic and structural properties that can be precisely modified to optimize the selectivity and efficiency of CO_2 reduction reactions. This tunability enables the coupling of SWS and CO_2RR, which empowers researchers to design catalysts that optimize both reaction kinetics and product specificity, facilitating the conversion of CO_2 into valuable chemicals or fuels, such as carbon monoxide, methanol or formic acid.[16]

Despite significant progress, challenges remain in improving the stability, scalability, and efficiency of photoelectrocatalysts under real-world conditions. Research continues to focus on tailoring the local chemical environment, improving light-harvesting capabilities, and reducing the use of precious materials. As a multidisciplinary field, photoelectrocatalysis holds immense potential for addressing energy and environmental issues sustainably.[12–14]

4.3 Thin films

The preparation of efficient photoelectrodes is a crucial step in advancing photoelectrocatalysis for solar water splitting. Photoelectrodes, must be made from semiconductor materials that exhibit suitable bandgaps to meet the energy requirements for redox reactions, such as water oxidation. While both electrodes play vital roles, our focus is specifically on the preparation of photoanode materials. Thin-film fabrication techniques, such as dip-coating and evaporation-induced self-assembly (EISA), have emerged as pivotal methods for creating nanostructured photoanodes with enhanced surface areas and improved charge transport properties.[17]

Photoanodes are a central component of photoelectrochemical cells, where they play a critical role in enabling solar water splitting and other photocatalytic reactions. Acting as the site for light absorption and water oxidation, photoanodes must possess several key attributes, including strong light-harvesting capabilities, efficient charge carrier separation, and the ability to facilitate redox reactions at their surface. Their material composition, structural design, and electronic properties directly influence the efficiency and durability of the photoelectrochemical process.[18]

The use of thin films in photoanode design provides several advantages. Thin films offer the ability to precisely tailor the structural and morphological properties of the photoanode, including surface area, pore

distribution, and thickness. By reducing the distance that minority charge carriers must travel, thin films mitigate charge carrier recombination, a common challenge in photoelectrocatalysis. Furthermore, nanostructured thin films with mesoporous architectures increase the active surface area for reaction, which enhances the contact area between the semiconductor and the electrolyte. The mesoporosity allows for the creation of well-defined pathways for electron-hole migration, which reduces charge recombination and improves charge carrier transport efficiency.[18]

Another advantage of thin film photoanodes is their adaptability to different fabrication techniques. These strategies also enhance the crystallinity of thin films, which is essential for effective light absorption and charge transport.[19]

Despite their benefits, thin films have limitations. While the reduced thickness of these films facilitates efficient charge transport, it is sometimes argued that they provide less material for light absorption. However, overly thick films can also be problematic because the lower layers may not significantly contribute to light absorption due to optical attenuation. This suggests that there is an optimal film thickness (100-150 nm) that balances sufficient material volume for absorption with effective charge extraction. Additionally, maintaining the stability of the mesoporous structure during high-temperature thermal treatments required for crystallization can be challenging. These processes may lead to pore collapse or unwanted phase transitions, which can negatively impact the photoanode's performance. Moreover, the durability of thin film photoanodes under operating conditions, particularly in harsh electrolytes or under extended illumination, remains a critical area for improvement.[20]

Thin film photoanodes are widely used for water splitting applications, where they drive the oxygen evolution reaction (OER) by utilizing photogenerated holes. Beyond water splitting, they are also employed in pollutant degradation and CO_2 reduction, showcasing their versatility. Their tunable properties and compatibility with various semiconductor materials, such as metal oxides and hybrid organic-inorganic structures, make thin films a cornerstone of research in sustainable energy technologies.[19,21]

4.4 Materials for Photoelectrochemical (PWS/SWS) Systems: Oxides and Oxynitrides

Photoelectrochemical water splitting (PWS) and solar water splitting (SWS) rely on the development of efficient photoanode materials that can absorb sunlight, generate charge carriers, and facilitate the oxidation of water. Among the various materials investigated, metal oxides and oxynitrides have emerged as promising candidates due to their unique electronic structures, stability, and abundance.[22]

Metal oxides such as TiO_2, Fe_2O_3, and WO_3 are well known for their robust chemical stability and favorable band edge positions for water oxidation. However, their relatively wide bandgaps can limit visible light absorption, thereby reducing their efficiency in PWS/SWS applications. In contrast, oxynitrides, which are derived from metal oxides by partially substituting oxygen with nitrogen, offer an attractive alternative. This substitution narrows the bandgap, enabling better utilization of the visible spectrum while largely retaining the material's chemical robustness.[22] General issue with oxides is that their band gaps are either too wide (most are white) or too narrow (good number of black oxides), but only a few are colorful, hence absorbing visible light (Cu_2O, $BiVO_4$). Nevertheless, introducing nitrogen doesn't always narrow the bandgap, there are cases where the opposite is true.[23]

The lower electronegativity and higher polarizability of nitrogen compared to oxygen lead to increased metal-anion bond covalency and a reduction in band gap, thereby promoting greater absorption in the visible spectrum. The synthesis of these materials is primarily carried out through ammonolysis, where oxide precursors react with ammonia at high temperatures to incorporate nitrogen into the crystalline structure. [22]

Alternative methods include pulsed laser deposition (PLD) and sputtering, techniques that are also relevant for the fabrication of NbO thin films. In fact, topotactic nitridation has proven to be an effective method for transforming oxide structures into oxynitride layers, reducing the band gap by up to 1.8 eV, a strategy that could be applied to optimize photoanodes.[24]

Oxynitrides have demonstrated significant potential in various technological applications, including use as inorganic pigments, dielectrics, and, more recently, photocatalysts for water splitting. Among the most researched and promising oxynitrides are perovskite-type materials such as $LaTiO_2N$, $CaNbO_2N$, and $BaTaO_2N$. These compounds are often considered among the best due to their favorable band gaps, robust chemical stability, and effective performance in photocatalytic water splitting. Consequently, integrating these oxynitrides into photoanode designs is viewed as a viable strategy to enhance both the efficiency and stability of photoelectrochemical devices.[25–28]

4.5 Thesis Motivation

The primary objective of this thesis is to advance the performance of photoelectrochemical cells by developing and adjusting novel photoanode materials. In particular, the work focuses on synthesizing and characterizing niobium oxide (Nb_2O_5) thin films due to their promising electronic properties, including a favorable band structure that enables efficient charge separation and enhanced light absorption. However, it is intriguing that oxynitrides, which have been widely studied as alternative photoactive materials, are not mentioned in the motivation. Recent studies suggest that substituting oxygen with nitrogen in Nb_2O_5 can lead

to significant modifications in the band structure, potentially narrowing the bandgap and shifting the band edge positions to more favorable values for water oxidation.[29]

Niobium-based materials are especially attractive for SWS because their conduction and valence band edges can be finely tuned via nitrogen incorporation, thereby enhancing charge separation and reducing recombination losses. Moreover, experimental studies on Nb_2O_5 have provided valuable insights into its band structure through techniques like X-ray photoelectron spectroscopy and density functional theory, supporting the rationale for exploring its oxynitride counterpart.[30] Investigating these NbO or Nb_2O_5-derived oxynitrides may thus offer a promising strategy to overcome the current limitations of conventional photoanode materials.[31]

5 Methodology

5.1 Thin film synthesis

5.1.1 Solution Preparation

Dip coating is a widely used method for thin film fabrication, employing a dip-coater machine (Surface Science Osslla Dip-Coater) to precisely apply coatings onto a substrate. This process involves depositing a liquid solution as a film through controlled immersion and withdrawal of the substrate at a defined speed. Its versatility makes it ideal for both industrial applications and research in advanced materials.[32]

The dip-coating process consists of five key stages:

1. Immersion: The substrate is introduced into the coating solution at a constant speed.
2. Dwelling: The substrate remains submerged for a set period to ensure proper adhesion of the coating.
3. Withdrawal: The substrate is extracted at a controlled speed, which directly influences the final film thickness.
4. Solvent Evaporation (Drying): The solution begins to dry as the solvent evaporates.
5. Curing: The film undergoes thermal and/or chemical treatment to stabilize its final properties.

The withdrawal and drying stages have the most significant impact on the coating properties, as they determine the final film thickness. This thickness also depends on factors such as solution viscosity and solid content. For withdrawal speeds above 0.1 mm/s, the Landau-Levich equation describes the relationship between film thickness and withdrawal velocity, considering surface tension at the liquid-air interface.[33]

$$h_0 = c\frac{(\eta U_0)^{\frac{2}{3}}}{\gamma_{LV}^{\frac{1}{6}}(\rho g)^{\frac{1}{2}}} \quad (4)$$

Where h_0 is the estimated thickness, c is a constant dependent on the curvature of the meniscus, η is the viscosity of the solution, U_0 is the withdrawal velocity, γ_{LV} is the surface tension at the liquid-air interface, ρ is the solution density and g is the gravitational constant.

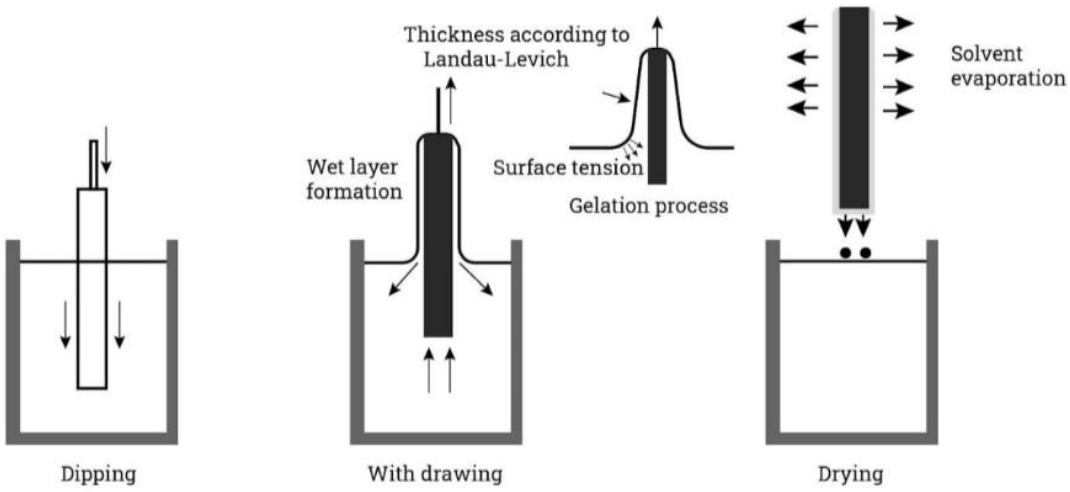

Figure 3: Dip-coating process. On the left, the dipping step. In the middle, the withdrawal and representation of the meniscus formation. On the right, the drying step[33].

The solution in which the substrate is immersed consists of $NbCl_5$, ethanol, Pluronic F-127, citric acid and distilled water (Table 1).

Table 1: Compounds (with their purity) needed to make the thin film solution.

Compound	Purity
Niobium (V) Chloride	≥99.9 %
Pluronic F-127	≥99 %
Citric Acid	≥99.5%
Ethanol	≥99.8%
Distilled Water	≥99.9 %

The preparation of the solution begins with mixing 211 mg of $NbCl_5$ in 0.8 mL of ethanol and mixing it until homogeneous for 5 minutes. The niobium chloride may not dissolve completely, and applying slight heat (T<40 ºC)can facilitate the dissolution.

Then in a separate container, 45 mg of P.F-127 (Pluronic F-127) are dissolved in a mixture of distilled water (1.3 mL) and ethanol (0.2 mL) and stirred until completely dissolved. Once the solution is homogeneous, 70.3 mg of citric acid are dissolved into it and stirred until homogenized again.

Once dissolved, the first prepared solution is added to the second one and stirred for at least half an hour to make sure it is completely mixed.

Once the solution is ready, it is placed in a 1.3 mL (of the solution previously made) container where the dip-coating is performed (Figure 3). For this purpose, both silicon and FTO (Fluorine-doped Tin Oxide) substrates are prepared on which the niobium oxide layer is deposited.

Commercial quartz glass substrates covered with a layer of indium doped-tin oxide (ITO) (25 × 15 mm and 10 × 10 mm) (Figure 4) are used in this work, applying the same coating for subsequent PEC tests. To enhance surface adhesion, the cleaning process involves a solution composed of 99% ethanol and 1% polyvinylpyrrolidone (PVP) (Table 2). This mixture is applied to the quartz glass using dip-coating. Once dried, the substrates undergo dip-coating with niobium (precursor solution), following the same procedure as for silicon.

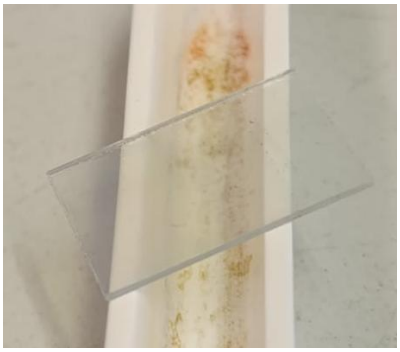

Figure 4: Quartz glass substrate.

Table 2: Polyvinylpyrrolidone.

Compound	Purity
Polyvinylpyrrolidone	≥99.9 %

5.1.2 Substrate Preparation

Starting with the silicon substrate, which is a semiconductor with a specified crystal orientation (1 0 0). The shiny surface of the material has two main characteristics, it is flat with some irregularities, and it is conductive, which makes it a perfect candidate as a substrate to deposit thin films and a good medium for SEM images.

The substrate is sold commercially as a disk of diameter 150 mm and thickness of 0.6 mm. This must be cut and cleaned before the dip-coating process. The silicon substrates utilized have a width and height of 15 x 25 mm.

To prepare the substrate, a ruler and a diamond-tipped pencil are used to mark the area where no reflection of the silicon was observed on the edge of the disc. Wafer pliers were then used to apply light pressure, creating a clean cut along the entire length of the disc in the preferential orientation. The process was repeated in the non-preferential orientation with slightly more pressure to ensure the silicon split cleanly (Figure 5).

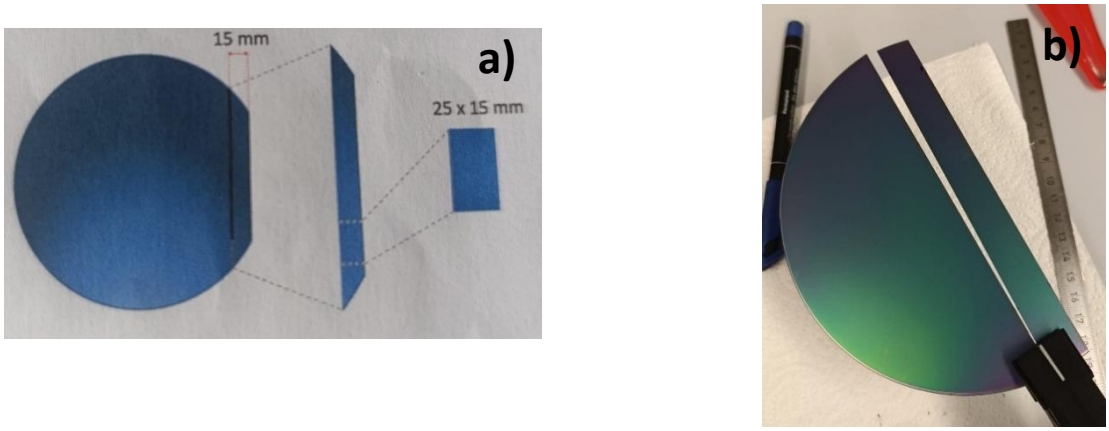

Figure 5: On the left (a) representation of surface preparation, on the right (b) longitudinal cut of the silicone disc.

All necessary substrates are first cleaned of dust by using a nitrogen gun. The substrates are then immersed in a 1:1 ethanol/acetone solution in a beaker, which is subsequently sonicated for 15 minutes in an ultrasonic bath (Figure 6). Thereafter, the surfaces are thoroughly cleaned with a high-precision cloth and dried using the nitrogen gun. Finally, the substrates are treated in an ozone cleaner for 10 minutes (Figure 7).

Figure 6: Ultrasonic bath.

Figure 7: Ozone cleaner.

The FTO substrates are purchased with defined dimensions, 25x15x1 mm. In this work, FTO is normally used for electrochemistry and UV-Vis spectroscopy experiments.

These substrates are glass coated with a metal oxide (Fluorinated Tin Oxide). Its main attributes are transparency, conductivity, and the fact that it is a low-resistant material. Hence, it can be used in the preparation of thin films for electrodes applied in photoelectrochemistry or photovoltaics cells.

It is necessary, in FTO, to recognize the conductive face and properly clean its surface, before carrying out the dip-coating process.

First, it is necessary to determine which of the two faces is the conductive one, for this a multimeter is used in resistance mode (Ω). Once the conductive layer has been checked, the same cleaning steps applied to the silicon substrate are performed.

Finally, in the case of quartz glass, it is also necessary to determine the conductive face and perform the cleaning/enhanced adhesion treatment previously explained. Quartz glass is used instead of FTO because FTO is not stable at the high temperatures required for the ammonolysis of niobium oxide (it would be destroyed). Therefore, a substrate that can withstand these conditions is needed.

5.1.3 Dip-coating process

The dip-coating process for the creation of thin films is carried out in a machine that consists of several parts, including tongs for gripping the substrate when submerged and drying, a capsule that maintains the humidity stable (which must be around 25% humidity for the process to be carried out properly) and a tube through which dry air enters and is used to regulate the humidity inside (Figure 8):

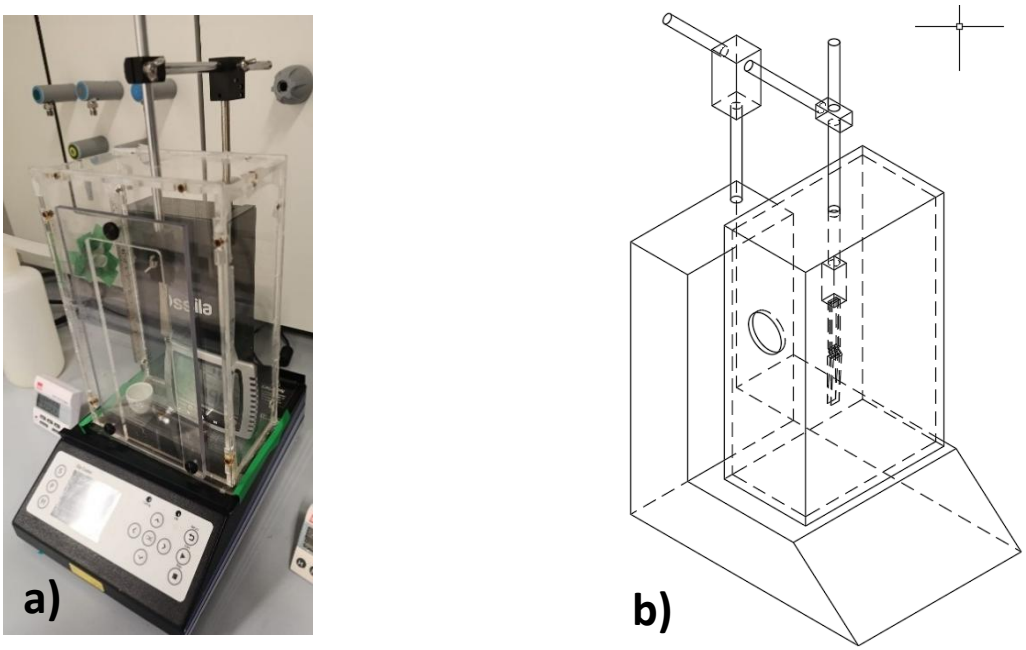

Figure 8: On the left (a) dip coating machine, on the right (b) model of the dip coater.

The parameters to be controlled when dip-coating are the immersion and withdrawal speed (where the withdrawal rate determines the thickness of the thin film), the height at which the substrate is to be dip-coated and the humidity inside the machine. The drying process inside the dip-coater is 5 minutes. In this work, dip-coatings are made at speeds between 6 mm/s and 1 mm/s as seen in figure 9.

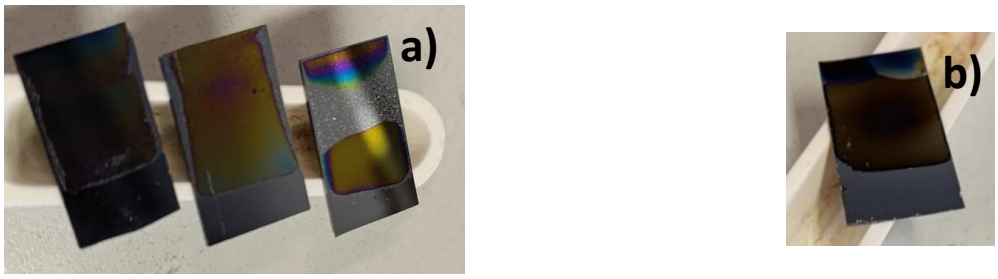

Figure 9: On the left (a) thin films at speeds 2, 4 and 6 mm/s, on the right (b) thin film at speed 1 mm/s.

5.1.4 Drying and powder preparation program

After dip-coating the thin films, they are placed in the oven preheated to 125 ºC and left to rest in the oven for 30 minutes. Once the time has elapsed, the following heating program is carried out (Figure 10):

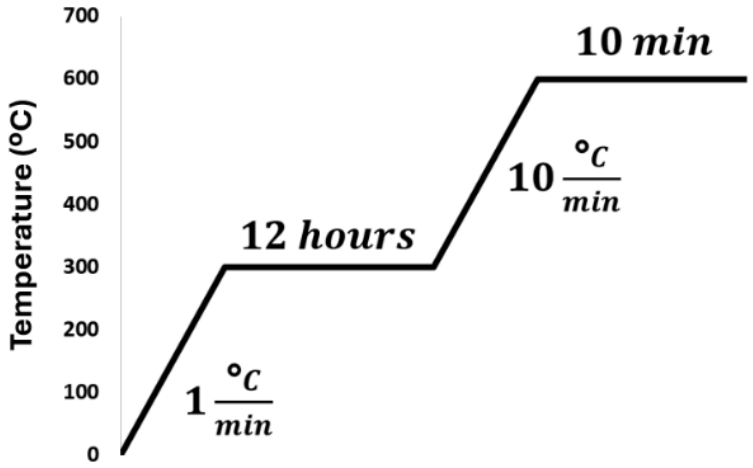

Figure 10: Furnace heating program.

At the end of the process, rapid removal from the oven is necessary to prevent polymer degradation due to heat. To obtain the powder, the solution used for dip-coating is placed in the oven after being dried for at least 12 hours in the dip-coater under dry air conditions and relatively low humidity (25% humidity). The resulting thin films exhibit the appearance shown in Figure 11:

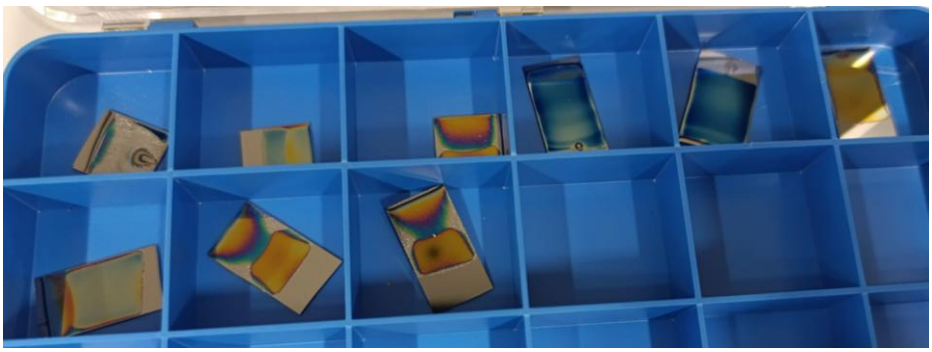

Figure 11: Thin films after drying process at different speeds.

To obtain the powder, use the same program used for the thin films, obtaining the result shown in Figure 12:

Figure 12: Niobium oxide powder.

For thin films synthesized on quartz glass, an initial drying step in the oven at 100 ºC for 10 minutes is required after the cleaning process to ensure that no residues remain on the surface. After this step, the dip-coating process is carried out in the same manner as for silicon substrates (Figure 13).

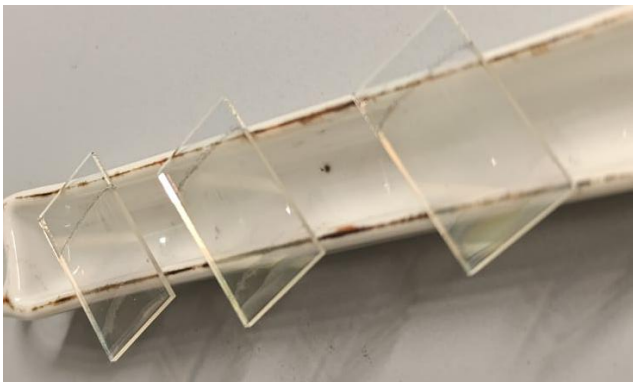

Figure 13: Quartz thin films (1 mm/s).

5.2 Ammonolysis

Ammonolysis is a chemical process in which a compound reacts with ammonia (NH_3), leading to the incorporation of nitrogen atoms into the material's structure. In the case of metal oxides, ammonolysis is an effective technique for converting oxides into oxynitrides or nitrides, depending on the reaction conditions. This process is widely used in the synthesis of advanced materials due to its ability to modify the structure and chemical composition of precursors, thereby enhancing properties such as conductivity, hardness, and corrosion resistance.

One of the main advantages of ammonolysis is its ability to precisely control the conversion of oxides into nitrides, tailoring electronic and mechanical properties. It is a versatile method applicable to various materials, allowing for adjustments in synthesis conditions to obtain different phases may be that the inherent mesoporosity of the material—providing a higher contact area with ammonia (enhances the ammonolysis process, rather than the process itself facilitating the formation of mesoporous structures). This increased

contact area ultimately contributes to improved reaction efficiency, which is advantageous for catalytic and electrochemical applications.[34]

A notable example of this process is the ammonolysis of niobium pentoxide (Nb_2O_5), a key precursor for the synthesis of niobium nitrides. The transformation of Nb_2O_5 through ammonolysis occurs in several stages, depending on temperature. During the ammonolysis of niobium oxide powders, β-Nb(O,N) forms at temperatures below 800 °C, with a nitrogen content of 13.0–13.6 wt% and an oxygen content of 4.5–5.0 wt%. At temperatures between 800 and 850 °C, NbO_2 is observed, while above 850 °C, the predominant phase is hexagonal NbN. This information is particularly relevant given that syntheses in this study were conducted at 800 °C. However, these findings specifically refer to powder samples, and phase evolution in thin films may differ due to variations in reaction kinetics and diffusion behavior.[35]

The conversion of Nb_2O_5 to niobium nitride can follow two different pathways. In one step, Nb(O,N) is directly formed, while in a two-step process, NbO_2 serves as an intermediate before complete nitridation into NbN. Research has shown that using mesoporous precursors with a high specific surface area accelerates ammonolysis and improves the quality of the final product. Additionally, the resulting porosity of the NH_3-treated material enhances its potential applications in catalysis and energy storage.[36]

The main objective of ammonolysis in this work is to reduce the bandgap of Nb_2O_5, forming $Nb_2O_{5-x}N_y$ structures that enhance the material's activity under a broader range of light intensities and improve electron conductivity. This process aims to extend the material's absorption into the visible range, making it more effective for applications that require visible-light activity. Figure 14 illustrates the schematic representation of how ammonolysis affects the electronic band structure:

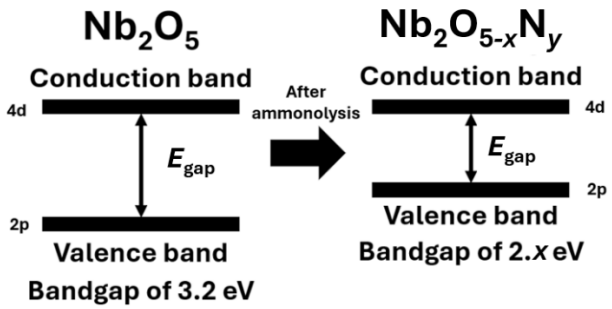

Figure 14: Effect of the ammonolysis on the material's band gap and band edges.

In this work, a single thin film is introduced into each tube furnace (Figure 15a). The furnace is sealed and the air inside is purged with an argon flow. After 5 minutes, the argon flow is stopped and an ammonia flow (100 ml/min) is activated. The temperature is then allowed to increase gradually up to 800 °C, where it is maintained

for 3 hours. Finally, the temperature is allowed to decrease back to room temperature. Before removing the thin film (Figure 15b), the atmosphere is once again cleaned with an argon flow.

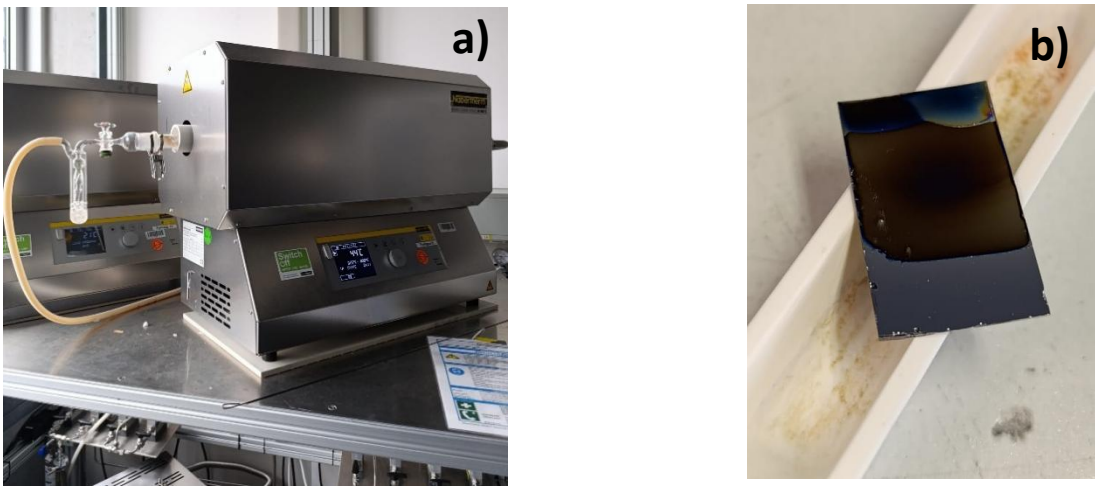

Figure 15: On the left (a) ammonolysis furnance, on the right (b) ammonolized silicon thin film.

5.3 Characterization Methods

5.3.1 Analysis with XRD

X-ray diffraction (XRD) (Figure 16) is a fundamental technique in the characterization of crystalline materials, based on the elastic scattering of X-ray radiation by the electron density in of a material. When a monochromatic X-ray beam strikes a crystal, the electrons of the atoms scatter the radiation in all directions. Due to the periodicity of the crystal lattice, constructive interference occurs at specific angles, generating a characteristic diffraction pattern.

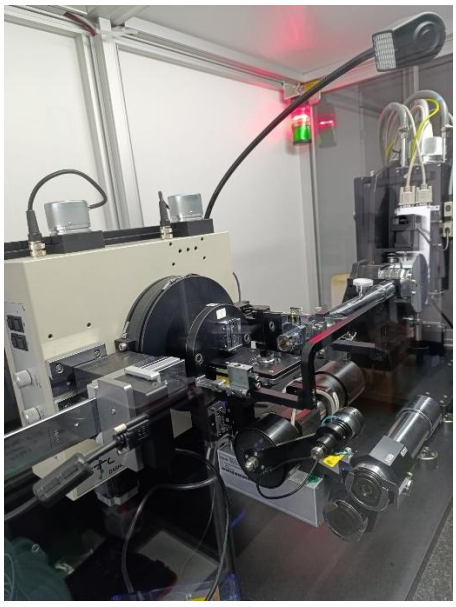

Figure 16: XRD machine in reflection mode.

This phenomenon is described by Bragg's law (equation 5):

$$n\lambda = 2d_{hkl}sin\theta_{hkl} \quad (5)$$

Where *n* is the order of diffraction, λ is the wavelength of the incident radiation, d_{hkl} is the interplanar spacing of the crystal planes with Miller indices *hkl*, and θ_{hkl} is the diffraction angle.

The diffractometer measures the intensity of the diffracted X-rays as a function of the 2θ angle, generating a diffraction pattern that provides key information about the material's crystal structure. By analyzing the position, intensity, and shape of the diffraction peaks, it is possible to determine lattice parameters, space group, phase composition, and microstructural defects such as residual stresses and crystallite size.

Due to its ability to identify crystal structures and analyze polycrystalline materials, XRD is an essential tool in materials science and engineering, widely used for phase identification and quantification, crystallographic texture evaluation, and internal stress characterization.[37]

For this work the XRD has 2 modes, the reflection mode used to characterize thin films (Figure 16) and the transmission mode used to characterize powders (Figure 17).

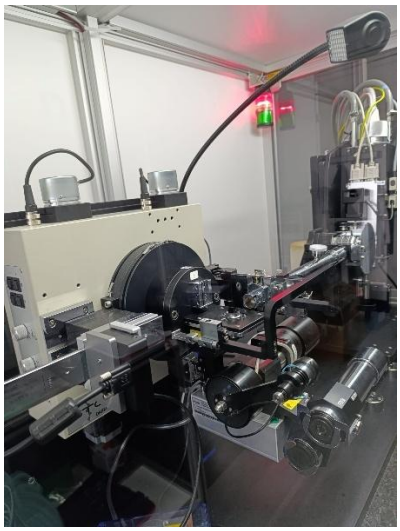

Figure 17: XRD on transmission mode.

The radiation used in our X-ray diffractometer comes from a molybdenum source. Powder X-ray diffraction measurements were carried out using a STOE STADI MP X-ray diffractometer to analyze the atomic structure and phase purity of all the powder samples. The measurements were performed using Mo-Kα1, radiation in transmission and reflection geometries, with a continuous scan covering an angular range of 5º ≤ 2 θ ≤ 48º. For the discussion of the data, it is convenient to convert this to the copper source wavelength, as it is the most widely used in the literature for our materials, for which Equation 6 is applied.

$$\lambda(Cu) = 2.17373939\,\lambda(Mo) \tag{6}$$

Other parameters used in the measurement are a grazing incidence angle of 0.4º and a range of 2θ between 0º and 48º.

5.3.2 Analysis with Raman Spectroscopy

Raman spectroscopy (Figure 18) is an optical technique based on the inelastic scattering of light, used to characterize the molecular structure of materials. When a monochromatic light beam, typically from a laser, interacts with a sample, most of the radiation is elastically scattered (Rayleigh scattering). However, a small fraction of the light undergoes frequency shifts due to interactions with the vibrational modes of the molecule, resulting in Raman scattering.

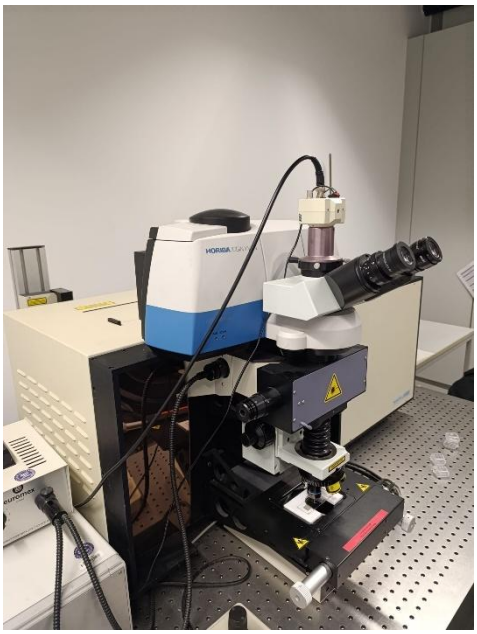

Figure 18: Raman Spectroscope.

The frequency shift of the scattered light depends on the molecular vibrations of the material and is described by the Raman frequency equation (equation 7):

$$\Delta v = v_{incident} - v_{scattered} \tag{7}$$

Where Δν is the Raman shift, $v_{incident}$ is the frequency of the laser radiation, and $v_{scattered}$ is the frequency of the scattered light. This shift is characteristic of chemical bonds and molecular symmetry, allowing for material identification and structural analysis.

A typical Raman spectroscopy system consists of:

- Excitation source: A laser providing monochromatic light.
- Dispersion system: Typically, a spectrometer with a diffraction grating to separate the scattered wavelengths.
- Detector: Commonly a charge-coupled device (CCD) to record the spectral signal.

The resulting Raman spectrum displays characteristic peaks that can be analyzed to determine the chemical composition, crystalline structure, and physical state of a material. The technique is widely used in materials science, nanotechnology, and the chemical industry due to its ability to provide non-destructive and highly specific information.[38]

To perform the analyses on both powders and thin films, very specific experimental parameters were used. In both cases, a 514 nm green laser (or 515 nm in Raman instrumentation) was used, together with precise filters and optical components: in the initial measurements, a 0.3 mm diameter filter, a micrometer-sized slit and orifice, and a x50 LWD objective were used, each measurement being performed once for 10 seconds and repeated 10 times; while, for Raman spectroscopy, a HR800 Horiba Jobin-Yvon spectrometer with a 50x/0. 50 objectives, configured with 10 accumulations and 10 seconds of integration in the point scans, together with an intensity filter of 0.06. In addition, a light microscope was used to position and direct the samples, which allowed obtaining chemical and structural information, and the identification of the components of thin films.

5.3.3 Analysis with SEM

Scanning electron microscopy (SEM) (Figure 19) is a widely used characterization technique in materials science and geology for analyzing the morphology, topography, and chemical composition of solid samples at the micro- and nanoscale. Unlike optical microscopy, SEM employs an electron beam instead of visible light to obtain high-resolution images of material surfaces.[39]

Figure 19: Scanning electron microscopy (SEM).

SEM operates by directing a focused beam of accelerated electrons onto the sample. These electrons interact with the material in various ways, generating signals that provide structural and compositional information. The most relevant detected signals include[39]:

- Secondary electrons (SE): Emitted from the sample surface, providing detailed topographical information.
- Backscattered electrons (BSE): Reflected incident electrons that reveal compositional contrast based on atomic number.
- Characteristic X-rays: Emitted when electrons displace inner-shell electrons of atoms, enabling chemical analysis via energy-dispersive X-ray spectroscopy (EDS).

A typical SEM system consists of[39]:

- Electron source: Can be a tungsten filament, LaB_6 cathode, or a field emission gun (FEG), which determines the resolution of the instrument.
- Electromagnetic lenses: Focus the electron beam onto the sample.
- Detectors: Capture the generated signals to produce images or chemical composition spectra.
- Vacuum system: Maintains a contamination-free environment to prevent electron scattering.

In this work, the primary objective of the SEM analysis is to examine the morphology of the thin film, specifically its porosity, surface organization, and the presence of any additional structures. Additionally, the SEM is used to assess the existence, size, and distribution of pores. The images were obtained using a JEOL 7600F microscope in Secondary Electron Imaging (SEI) mode, using 20 kV acceleration voltage, with magnifications ranging from approximately 150,000x to 400,000x.

5.4 UV-Vis Spectroscopy

Ultraviolet-visible (UV-Vis) spectrophotometry is an analytical technique based on the absorption of radiation in the ultraviolet (UV) (190-400 nm) and visible (Vis) (400-700 nm) regions of the electromagnetic spectrum. This absorption occurs when electrons in a molecule or compound transition from a ground state to an excited state. The amount of light absorbed at different wavelengths provides information about the concentration and structure of the analyte.

Beer-Lambert's law describes the relationship between absorbance and the concentration of a substance, which applies not only to solutions but also to solid-state materials, as in this study (Equation 6)[40]:

$$A = \varepsilon c l \tag{8}$$

Where *A* is the absorbance, ε is the molar absorption coefficient (L mol^{-1} cm^{-1}), *c* is the concentration of the sample (mol/L) and *l* is the optical path length (cm).

A UV-Vis spectrophotometer consists of several key components that work together to analyze a sample. The light source includes a xenon or deuterium lamp for the UV region and a tungsten-halogen lamp for the visible region. A monochromator then separates the light into different wavelengths using a diffraction grating or prism. The light passes through a cuvette, which holds the liquid sample in a quartz container for UV measurements or a glass/plastic container for visible light. The detector captures the transmitted light and converts its intensity into an electrical signal, typically using photodiodes or photomultiplier tubes. Finally, the processing and display system calculates absorbance and presents the data on a screen for analysis[40].

This characterization method is widely applied across disciplines, including chemical, biochemical, environmental, and food quality analyses. However, for this work, the most relevant application is in nanotechnology and materials science, specifically for the characterization of nanoparticles and optical coatings. This technique enables precise analysis of optical properties such as absorbance and transmittance, which are crucial for assessing material performance and stability. Additionally, it is particularly important in this study as it allows for estimating the bandgap, which is the main reason for its use.[41]

A PerkinElmer Lambda 365+ UV-VIS Spectrometer (Figure 20), capable of analyzing a visible and ultraviolet spectrum between 200 and 1100 nm wavelength, is used for this study. It highlights the use of a deuterium lamp in the ultraviolet region.

Figure 20: Spectrometer UV-VIS Lambda 365+.

The lamps are preheated 15 minutes before the measurement. During this time, both the reference sample and the sample to be measured are prepared. The reference sample is placed at the bottom of the device, while the sample to be measured is positioned on the near side (Figure 21). The reference sample consists of a substrate identical to the one used for the thin films under analysis.

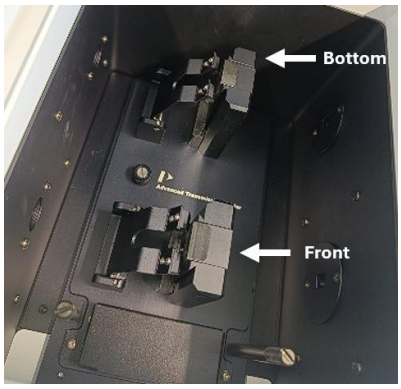

Figure 21: Spectrometer sample holders

The aperture width of the device is 1 mm (adjustable), with a scanning speed of 480 nm/min. The device provides a measurement for each nanometer of wavelength analyzed, with data recorded at intervals of 1 nm.

Thanks to this device, it is possible to obtain both absorption and transmission curves (they are complementary) that allow us to know how much light is absorbed or passes through the material, enabling an initial evaluation of the performance that will be obtained in PEC experiments, estimating the optical bandgap of the material.

5.5 XPS

X-ray emitted photoelectron spectroscopy (XPS) (Figure 22) is a characterization technique widely used in materials science and chemistry to analyze the chemical composition, oxidation states and chemical interactions at the surface of solid samples at the nanometer scale. Unlike optical or microscopic techniques, XPS uses X-rays

to induce photoelectron emission from the sample, allowing detailed information to be obtained about the chemical environment of each element present.[42]

Figure 22: XPS device used.

XPS operates by irradiating the sample with X-rays (usually from Al Kα or Mg Kα sources), which causes the emission of photoelectrons. The kinetic energy of these photoelectrons is measured and converted into binding energies, which are characteristic of each element and its chemical state. The XPS spectrum reveals elemental identification through main peaks from photoelectron emission, oxidation states via satellite peaks, and allows for more accurate analysis by correcting the inelastic background from energy losses.[42]

An electron analyzer, usually a hemispherical spectrometer, which measures the kinetic energy of the photoelectrons and allows reconstruction of the binding energies; a detector, responsible for recording the signal of the analyzed photoelectrons and generating the corresponding spectrum; and a vacuum system, which maintains a low-pressure environment to avoid scattering of the photoelectrons and ensure accurate measurements.[43]

In this work, multiple samples are introduced into the XPS inlet of the DAISY-FUN system, a cluster tool equipped with a SPECS PHOIBOS 150 spectrometer featuring an Al Kα X-ray source (monochromatic Focus 500 with XR50 M, *hv* = 1486.74 eV). Each chamber is pressurized separately, and samples are manually transferred from one chamber to another until they reach the X-ray analysis station, where the necessary data is collected.[44]

5.6 PEC Tests

We start by preparing the samples by placing thin films on quartz glass and silicon substrates on a steel support plate, ensuring a robust electrical connection by means of a wire attached to the surface of each thin film. The experimental system (Figure 23) is mounted on a 3D printed cell designed to securely house the electrolyte and electrical components:

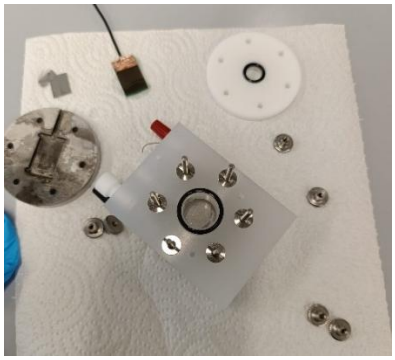

Figure 23: PEC Cell components.

A buffer for pH control based on a 7 pH Na_2SO_3 solution (0.2M Na_2SO_4, 0.1M KH_2PO_4, 0.1M K_2HPO_4 and 1M Na_2SO_3 (h+)) is introduced into the cell and an Ag/AgCl reference electrode is used. The electrical connection is made using three wires: the red wire is assigned to the cathode, the black wire is connected to the anode (directly to the thin film) and the green wire is used for the reference electrode, setting an offset of 0.636 V to maintain the required polarization during the experiments.

Subsequently, tests are performed by subjecting the samples to controlled irradiation with visible and ultraviolet light, while monitoring relevant electrochemical parameters such as current and voltage. This illumination is performed frontally on the surface (with an intensity of 1000 W/m^2 for visible light simulating sunlight and 500 W/m^2 for ultraviolet light.) in a closed black box so as not to allow other illumination to alter the results (Figure 24):

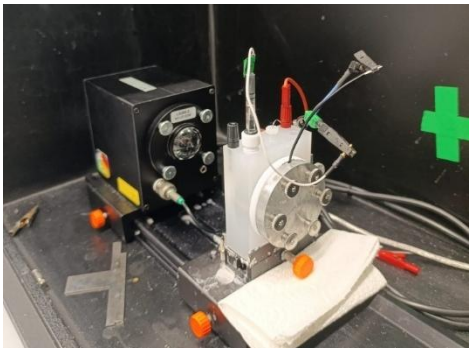

Figure 24: PEC prepared.

To collect the results, the potentiostat is directly connected to the computer which, thanks to a specific software, allows to adjust the amount of current applied (in this case between 1V and 3V) and other parameters such as the offset and the power of the bulb.

6 Results

6.1 XRD Results

6.1.1 XRD patterns of Nb_2O_5 powder

To begin with, it is necessary to know the composition of the thin film that has been made, for this purpose the powder formed by the calcination is analyzed, obtaining the following pattern (Figure 25):

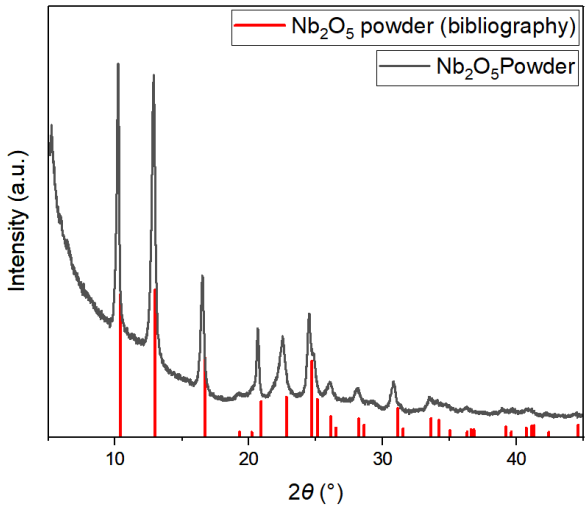

Figure 25: Comparison of the XRD pattern of the Nb_2O_5 powder (black) with that obtained in the literature (red).[45]

Comparing the results with the literature, its orthorhombic crystalline system with space group *Pbam* (55).[45]

It can be seen how in the literature the most intense reflection is at $2\theta \approx 13º$ (*hkl* = 131) followed closely by the one located at $2\theta \approx 10.5º$ (*hkl* = 001), being in the analyzed sample the opposite, but the rest of the reflection are quite similar to the pattern obtained in this work, this can occur in two ways, one being due to the presence of a different composition and the other (being the most likely) due to a prefered orientation.[45]

6.1.2 XRD patterns of silicon thin films

Initially, the XRD test is performed on the thin films deposited with withdrawal velocities of 1, 2, and 4 mm/s (Figure 26):

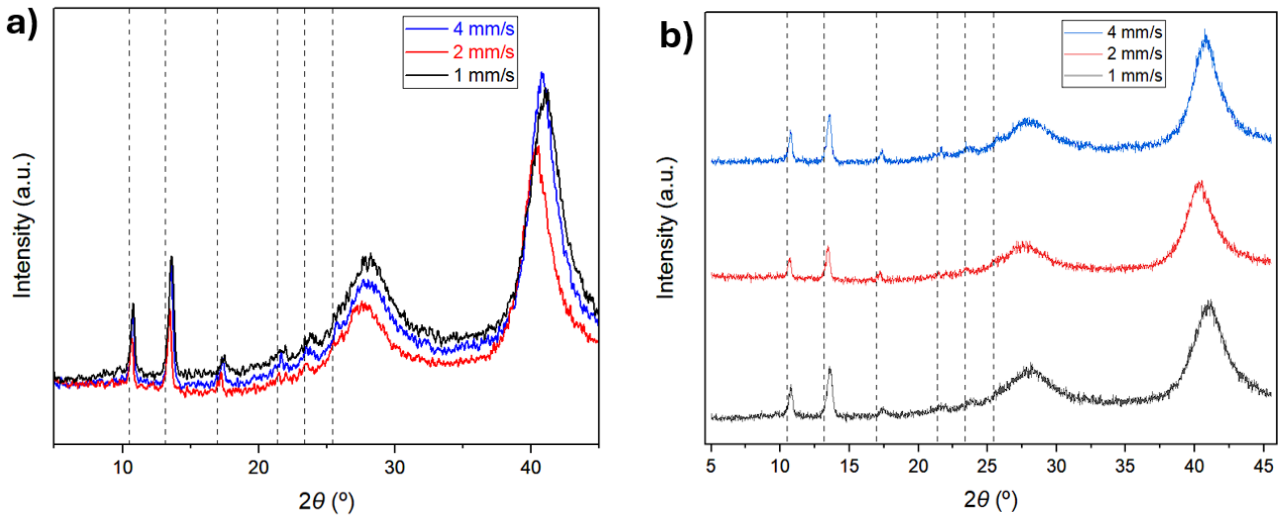

Figure 26: (a) superimposed XRD pattern of the 1 (black), 2 (red) and 4 (blue) mm/s withdraw velocity of the oxide thin films on silicon substrate compared with the reference pattern (dotted lines), (b) separate XRD patterns of the same thin films.

These measurements have been performed with an incidence angle of 1.2° in a range of 2θ between 5º and 45°, tests performed later in this work will demonstrate that these parameters are optimal for the measurement of these thin films.

As can be observed in the figure 26, multiple reflections of varying intensities are present, with the most notable reflections appearing at approximately $2\theta \approx 11º$ and $2\theta \approx 13º$. Using the Match! 4 software (ICDD database) and applying the conversion factor from molybdenum to copper radiation (equation 6), it was determined that Nb_2O_5 is present in the thin film.

The XRD patterns of the Nb_2O_5 thin films exhibit broad reflections rather than sharp reflections, suggesting the presence of small crystallites and a low degree of crystallinity[46]. The detected phase corresponds to pseudohexagonal TT-Nb_2O_5 (JCPDS 00-028-0317), which is expected since the thermal treatment was performed at 600 °C for only 10 minutes. This phase is typically formed at around this temperature, confirming the structural characteristics of the obtained films[47].

It can also be seen that although all the coating speeds have similar intensities, the results obtained with the speed of 1 mm/s are somewhat more accentuated than the other two speeds, therefore it could be said that the formation of Nb_2O_5 is preferentially under these conditions.

The two most intense reflections that appear at the end of the graphs correspond to the silicon substrate (Figure 27), because the thin film is very thin (between 100-200 nm), and the beam crosses the layer and measures the substrate in a very accentuated way:

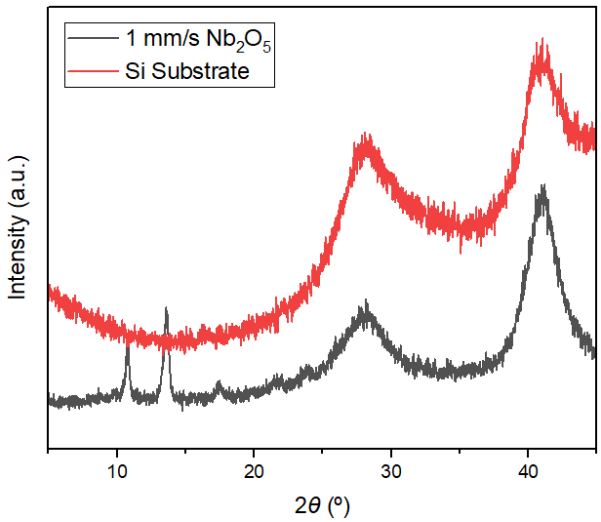

Figure 27: Comparison of the XRD pattern of an oxide thin film preapred with 1 mm/s withdrawal speed (black) and a silicon bare substrate (red).

To verify that the angle of incidence was appropriate, initial measurements were performed at two distinct reflection angles (specifically at 0.8° and 1.5°). The data obtained at these extreme angles were found to be less reliable, so additional measurements were conducted at intermediate angles of 1.0° and 1.2°. The latter set of measurements provided more accurate and reproducible results (Figure 28):

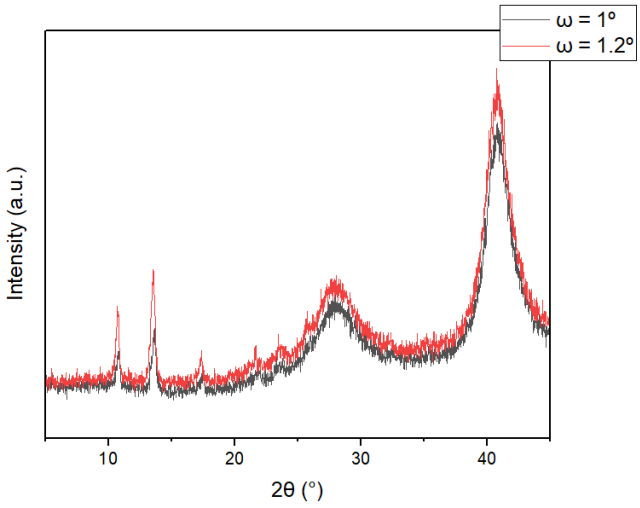

Figure 28: Comparison of the XRD pattern of an oxide thin film preapred with 1 mm/s withdrawal speed at 1° angle of incidence (black) and 1.2° (red) .

It can be seen that at an angle of incidence of 1.2° the intensity of the reflection is more pronounced, therefore all the experiments in this work have been carried out with this parameter and will be continued with this parameter.

To synthetize the aimed oxynitride for PEC tests, the oxide thin films are ammonolyzed. To see the evolution of the XRD patterns, a thin film without ammonolysis (oxide), one ammonolyzed at 800 ºC for 3 h, and

another undergoing the same treatment but without the constant flow of ammonia flowing through the furnace (treated in air) were compared, thus obtaining the following results (Figure 29):

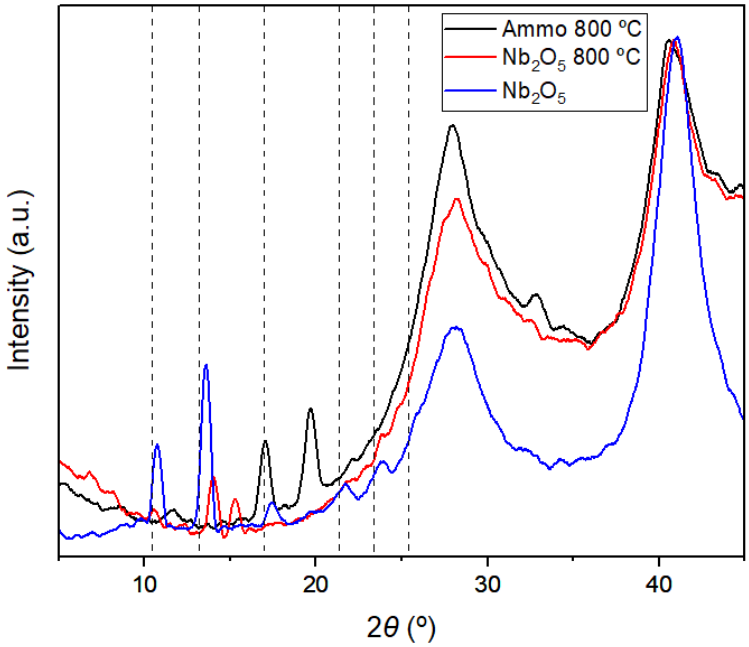

Figure 29: Normalized comparison of XRD patterns of 3 thin films: oxide (blue), oxynitride 800 ºC (black), oxide treated in air using the same temperature parameters of ammonolysis (red).

Although the larger ionic radius of nitrogen should theoretically expand the lattice and increase the interplanar spacing (thereby shifting the diffraction reflections to lower 2θ values according to Bragg's law) in practice, additional structural and chemical factors (such as local distortions, stress effects, and changes in bonding configurations) can counteract this expansion, resulting in shifts in the opposite direction.

Instead of forming a simple oxynitride (Nb-O-N) with lattice expansion, it is possible that substoichiometric or mixed phases (e.g., $Nb_2O_{5-x}N_y$) may be generated, whose lattice parameters may be smaller than those of pure Nb_2O_5. These substoichiometric phases arise due to partial oxygen substitution and/or lattice vacancies, which may induce a global cell shrinkage and be reflected in a shift of the reflections to higher angles.[48]

The reducing atmosphere of NH_3 can favor the reduction of Nb^{5+} to lower oxidation states (e.g., Nb^{4+} or Nb^{3+}). When the metal cation is reduced, its effective radius tends to increase, causing lattice expansion. This effect can add to the possible expansion caused by nitrogen incorporation, resulting in diffraction reflections at higher values of 2θ.[49]

Heat treatment under air vs. ammonia conditions can generate different residual stresses in the thin film. Densification, growth of crystalline domains or grain reorientation can slightly modify the lattice parameters,

manifesting in the shift of reflections. In addition, the introduction of point defects (oxygen vacancies, nitrogen interstices, etc.) influences the microstructure and can induce internal stresses that modify the interatomic distances.[50]

Not always all incorporated nitrogen enters homogeneously into the Nb_2O_5 network. N-rich regions, amorphous or semi-crystalline phases and concentration gradients may exist in the film. If the proportion of nitrogen in the primary crystalline phase is lower than expected, its lattice-expanding effect might not adequately counteract the contraction caused by niobium reduction and other defects. This imbalance could lead to an overall shift of the diffraction reflection toward higher angles.[50]

Nb_2O_5 exhibits multiple polymorphs (pseudohexagonal, orthorhombic, tetragonal, etc.), each with different cell parameters. Under treatment in air, the stable form may differ from that obtained by heating in NH_3 atmosphere. If the ammonolysis process promotes the transition to a polymorph with lower lattice parameters, this would explain the shift of the reflection to higher angles.[51]

Therefore, additional experiments (such as XPS) are performed on thin films made on the quartz glass substrate to more precisely determine their composition. This is crucial for subsequent PEC tests, especially since previous studies indicate that this substrate does not yield optimal results in this area. [51]

Finally, several thin films subjected to ammonolysis at different temperatures were compared to determine the optimum conditions and verify if the resulting XRD patterns conformed to expectations. In ammonolysis, it is generally anticipated that the reflections of the precursor oxide remain similar but shift toward lower angles due to lattice expansion from the incorporation of larger nitrogen ions as long as no structural transition occurs. In this context, the Nb_2O_5 reflections were expected to remain largely unchanged overall, with a more distinct reflection emerging at 800 °C (the target temperature) (at $2\theta \approx 11º$) (see Figure 30). Testing a range of temperatures allowed the researchers to assess whether this characteristic shift occurred or if the pattern changed entirely, which would indicate degradation:

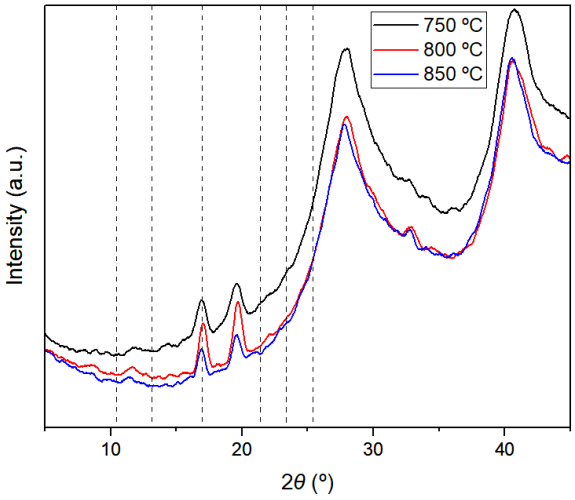

Figure 30: Comparison of XRD patterns of 3 oxynitride thin films at different temperatures (750 ºC (black), 800 ºC (red), and 850 ºC (blue)).

It can be seen how the displaced reflection of Nb_2O_5 are found in the same regions at the three temperatures, however, the 800 ºC treated sample has slightly more intense and more defined reflections than at the other two temperatures, so ammonolysis continued at that temperature throughout the work.

6.1.3 XRD patterns of quartz glass substrates

Now that the XRD analysis of both the thin film and the powder has confirmed the potential presence of Nb_2O_5, it is possible to better understand the composition of the obtained material, the XRD of the quartz glass deposited thin film with the same coating is performed, obtaining the following result (Figure 31):

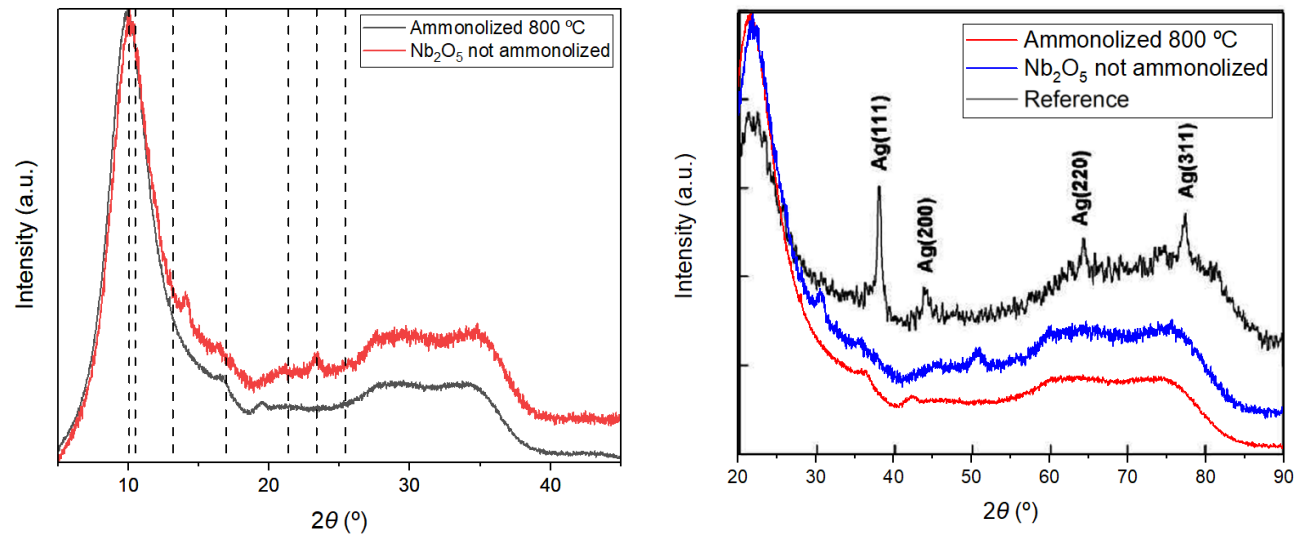

Figure 31: On the right comparison of oxynitride thin film (800 ºC) (black) with an oxide thin film (red) (a). As reference to identify the substrate contribution, a Ag thin film on quartz glass was selected (b).[52]

The first dotted line ($2\theta \approx 10º$) represents the quartz glass substrate as obtained in literature.[52] By comparing the results, it can be determined that this reflection corresponds to the quartz glass substrate.

Additionally, in the non-ammonolyzed thin films, the presence of Nb_2O_5 is faintly detectable, whereas in the ammonolyzed films, no clear features are observed, it should be noted that in figure 31b, the results obtained in this work have been converted to a copper source wavelength using equation 6.

The weakness of the Nb_2O_5 signal on quartz glass can be partly explained by the fact that, if the film is very thin, X-rays can pass through it and predominantly capture the contribution of the substrate. This leads to a diffracted signal where the intensity of the film is overshadowed by that of the quartz glass. Additionally, it is possible that the thin film on quartz glass is even thinner than on a silicon substrate, as suggested by the use of PVP to facilitate proper film formation on quartz glass.[53]

In addition, slight mismatches in the instrumental calibration or in the way the sample is mounted can cause shifts in the position of the reflections (2θ), making it difficult to match the theoretical values exactly. Finally, the nature of the quartz glass substrate (whether it is crystalline quartz with its own reflections overlapping those of Nb_2O_5 or quartz glass contributing a diffuse background) can mask or overlap the reflections in the film.[54,55]

Therefore, since XRD does not help in determining what material is deposited in the thin film or what material is obtained after ammonolysis, additional experiments such as XPS are performed to characterize the thin film.

6.2 Raman Results.

6.2.1 Raman spectroscopy for silicon substrates

Once the XRD analysis was completed, Raman spectroscopy was performed for the same thin films, obtaining the following results (Figure 32):

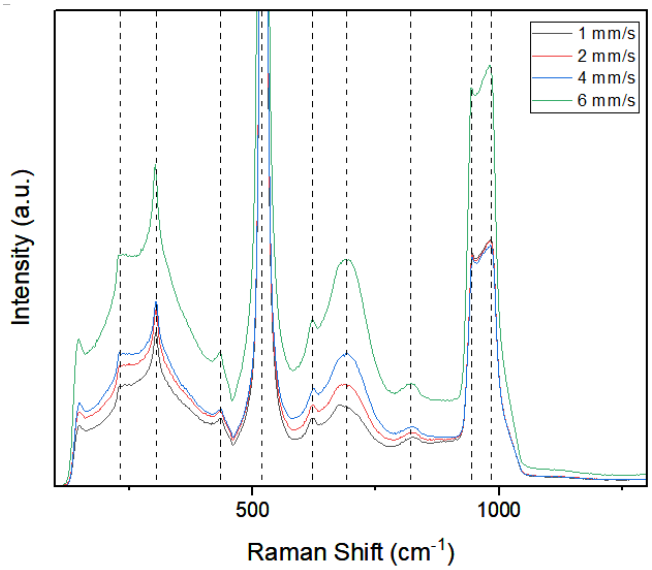

Figure 32: Raman spectra of the thin films deposited on silicon substrates at different withdrawal velocities 1 (black), 2 (red), 4 (blue) and 6 mm/s (green).

In the Raman spectra of the Nb_2O_5 thin films, very similar characteristic bands are observed around 231, 304, 435, 520, 622, 690, 820 and between 945 and 984 cm^{-1}, which correspond mostly to Nb_2O_5, as indicated by the positions reported in the literature.[56,57]

The bands between 230 and 305 cm^{-1} are attributed to the bending and stretching modes of Nb-O-Nb bonds, while the intense band at 690 cm^{-1} is associated with the symmetric stretching mode of Nb-O polyhedra, and the bands in the range of 945 to 984 cm^{-1} are assigned to the asymmetric and symmetric stretching modes of Nb=O surface groups, suggesting overlapping bands that may evidence the coexistence of multiple vibrational modes. [58–61]

In addition, peaks at 435 and 520 cm^{-1} are identified which, in the absence of substrate influence, are directly related to vibrational modes specific to Nb_2O_5, while the peak at 622 cm^{-1} could be linked to additional Nb-O modes. The intensity of all these peaks increases with acquisition speed (from 1 mm/s to 6 mm/s), suggesting that, as the density or thickness of the films increases, the Raman signal is enhanced. [58–61]

The definition and separation of the bands in the range of 945 to 984 cm^{-1} indicate an intermediate level of crystallinity, compatible with the presence of the pseudohexagonal phase (TT-Nb_2O_5). Although the spectra also agree with the coexistence of the orthorhombic phase (T-Nb_2O_5), the predominant is pseudohexagonal, as obtained in other deposition at 600 °C.[62–64]

Although it was seen that the intensity of the peaks increases with the withdrawal speed, the real difference is not too decisive, and the microscopic analysis has shown that all thin films produced above 1 mm/s have fractured.

After analyzing the Raman spectra of the oxide thin films, the thin films treated in ammonia were analyzed, obtaining the following results (Figure 33):

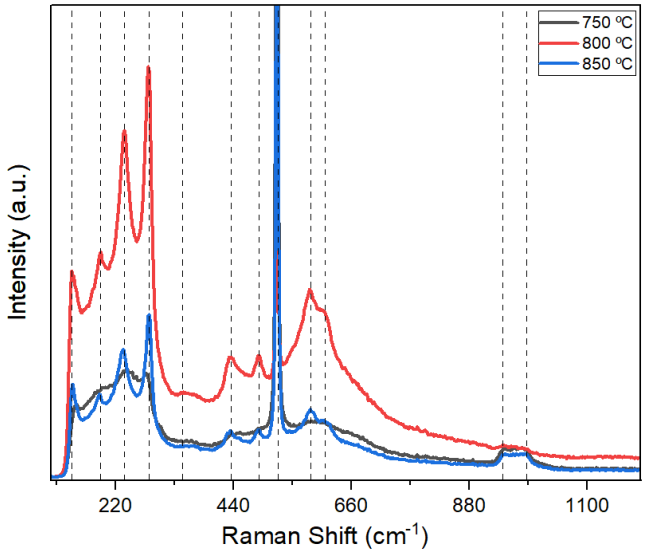

Figure 33: Raman spectra of the oxynitride thin films deposited on silicon substrates at different ammonia treatment temperature, 750 (black), 800 (red), and 850 ºC (blue).

With increasing ammonolysis temperature (from 750 to 850 °C), new bands appear and intensify in the low-energy region (below 400 cm^{-1}), as well as slight shifts or splits in typical Nb_2O_5 peaks (e.g, around 584 and 610 cm^{-1}), indicating the formation of oxynitride phases ($Nb_2O_{5-x}N_y$) and/or a partial transformation towards niobium nitride (NbN), in agreement with previous studies.[65,66]

In the sample treated at 750 °C, the new bands at low energies (138, 192, 237, 282 and 354 cm^{-1}) are less intense, suggesting a moderate degree of ammonolysis [65]. On the other hand, at 800 °C a clear increase of these bands is observed, accompanied by a broadening and shifting of the peaks in the 500-700 cm^{-1} region, revealing the coexistence of multiple local Nb environments and the more pronounced formation of Nb-O-N species [66]. Finally, at 850 °C, the intensity of the peaks corresponding to Nb=O (942 and 987 cm^{-1}) is slightly reduced, while the low-energy bands increase markedly, suggesting that the structure is moving towards a more nitrogen-rich phase, with possible further disorder in the crystal lattice.[67]

Notably, the band at ~523 cm^{-1} is associated with the silicon substrate, and is identified in all samples, although it may overlap with the Nb_2O_5 signal around 520 cm^{-1}.[68]

The persistence of characteristic Nb_2O_5 peaks (435 cm^{-1} and the 900-1000 cm^{-1} region) at all temperatures indicates that not all the oxide is completely transformed and that several phases (oxynitride, nitride and residual Nb_2O_5) may coexist [65,66]. These results agree with previous reports on the conversion of niobium oxides in ammonia atmosphere, where intermediate phases and a progressive substitution of O for N are observed as temperature and treatment time increase.[66,67]

Raman analysis of Nb_2O_5 thin films subjected to ammonolysis at increasing temperatures (750, 800, and 850 °C) reveals significant modifications in the material's vibrational modes. The spectra indicate a gradual formation of oxynitride and nitride phases, as evidenced by the emergence of new low-energy bands and shifts in the characteristic Nb_2O_5 peaks (e.g., in the 500–700 cm^{-1} and 900–1000 cm^{-1} regions). These changes suggest a progressive incorporation of nitrogen and the development of intermediate phases, including oxynitride and, to a lesser extent, niobium nitride. Nevertheless, the persistence of certain bands characteristic of Nb_2O_5 indicates that the transformation is incomplete, resulting in the coexistence of multiple phases and reflecting the complexity of the ammonolysis process.

6.2.2 Raman spectroscopy for powders

In turn, the Raman spectra of the Nb_2O_5 powder obtained by calcination of the solution used to obtain the thin films. Is analyzed to see the peaks present (Figure 34):

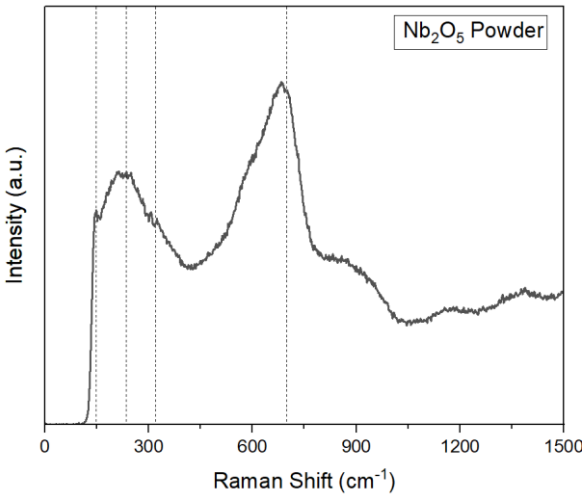

Figure 34: Raman spectra of the FTO (4 mm/s).

It is observed that the peaks in the low region (below 400 cm^{-1}) correspond to the translation and bending modes of the atoms in the crystal lattice, in which the Nb-O interaction generates collective vibrations. These modes are very sensitive to the crystal structure and to changes induced by heat treatment processes or the presence of impurities such as residual carbon.[69]

The intermediate region, approximately between 500 and 700 cm^{-1}, has bands associated with Nb-O-Nb bridge vibrations and structure deformations. In crystalline samples, peaks are observed around 584 and 610

cm^{-1}, although these can undergo shifts or broadening in the presence of defects or when nitrogen is incorporated into the lattice, giving rise to oxynitride phases ($Nb_2O_{5-x}N_y$).[70]

Finally, in the high region (900 - 1000 cm^{-1}), the Nb=O terminal stretching modes are located. Typical peaks around 942 and 987 cm^{-1} are attributed to these stretches and are very sensitive to the presence of excess oxygen or phase transformations. Given that the powder under analysis is a pure oxide (Nb_2O_5) that has not undergone any ammonia treatments, the observed attenuation or shift of these bands is attributed solely to the removal of carbonaceous impurities during prolonged calcination. This process can facilitate the formation of a mixed-phase material, without involving any nitriding processes.[69,70]

To try to eliminate the grayish color of the sample that possibly indicates the presence of carbon in the sample, we proceed to calcine the powder for 20 minutes more at 600 ºC and to make another sample without citric acid, thus obtaining two completely white powders that are analyzed next (Figure 35):

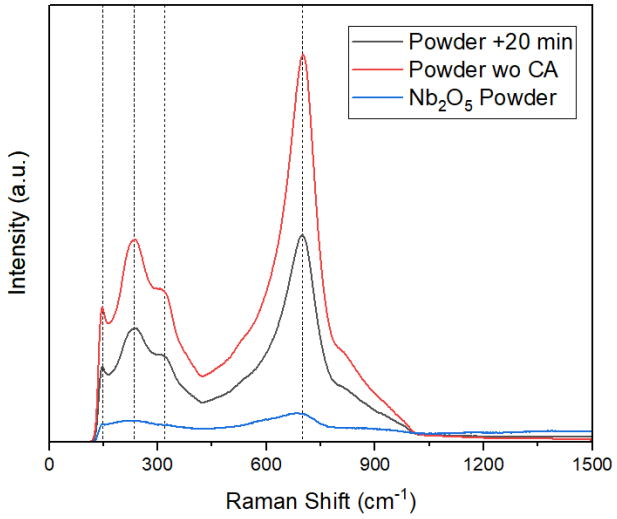

Figure 35: Raman spectra of three powders, the first one synthesised as described in the methodology part of this work (blue), the second one without citric acid (red) and the third one with a treatment at 600 °C 20 minutes longer (black).

The difference in color between the grayish powder and the white powder reinforces the spectroscopic interpretation: in the grayish powder, the possible presence of residual carbon (or the interference of carbonaceous compounds) attenuates and masks part of the Raman signal characteristic of Nb_2O_5, while in the white powder, obtained after a longer thermal treatment or in the absence of citric acid during the synthesis, the removal of carbon favors the clear detection of the bands characteristic of Nb_2O_5, presenting much more intense peaks. This shows that a longer treatment is effective in removing carbon impurities and thus enhancing the Raman signal of the oxide.

6.2.3 Raman spectroscopy for FTO

In turn, the spectroscopy for the FTO substrate will be analyzed to see the differences and similarities with the silicon substrate (Figure 36):

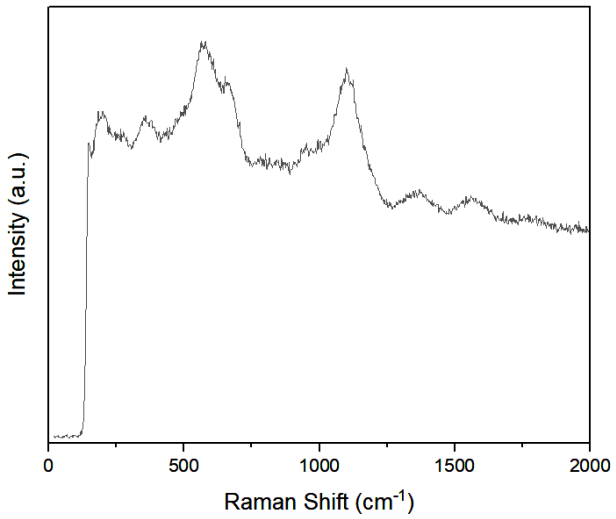

Figure 36: Raman spectra of the FTO (4 mm/s withdrawal speed).

When analyzing the Raman spectrum of our sample, we observed only signals corresponding to the FTO substrate, with no clear indications of the presence of the Nb_2O_5 thin film. Nb_2O_5 thin films deposited on FTO substrates exhibit features of TT-Nb_2O_5 and T-Nb_2O_5 phases, due to the similarity in their Raman spectra. In the literature, Nb_2O_5 was synthesized by the Pechini method and the orthorhombic phase was observed in samples calcined at 600 °C for 2 hours, with analysis of Raman spectra showing the vibrational characteristics of the structure obtained.[71] In this work, the absence of signals attributable to the thin film in the Raman spectrum suggests that we cannot confirm its presence or determine its structure by this technique.

6.2.4 Raman spectroscopy for quartz glass substrates

As for the other materials, quartz glass can also be analyzed by this technique, obtaining the following results (Figure 37):

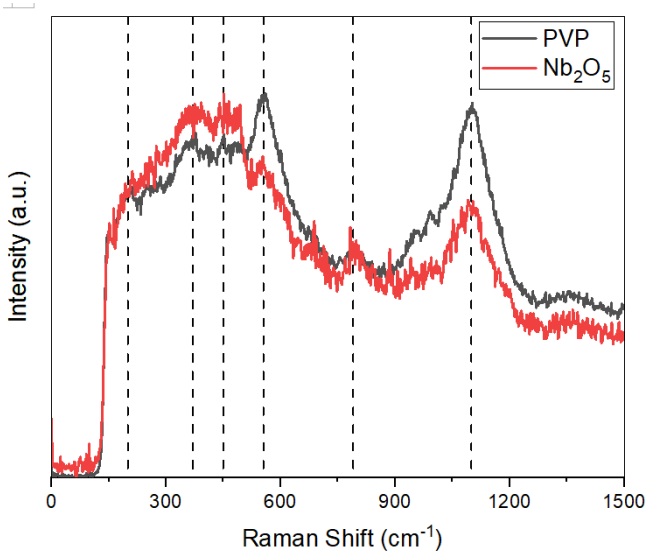

Figure 37: Normalized comparision of raman spectra of two quartz glass sustrates, one with only PvP (black) and the other one with PvP and Nb_2O_5 (1 mm/s) (red).

For example, a broad band around 440 cm^{-1} is observed in silica, attributed to the symmetric motion of bridging oxygens in the SiO_2 lattice. Likewise, bands are identified in the 200 cm^{-1} range (related to translational and bending modes) and in the high region (~790-1100 cm^{-1}), associated with asymmetric and symmetric stretching of the Si-O [72]. These studies support the hypothesis that, when a thin Nb_2O_5 film is deposited on quartz substrates, the Raman laser heavily penetrates the film, and the substrate signal is essentially detected. As a result, a decrease in the intensity of the characteristic quartz glass peaks is observed, without significant changes in their position.

Finally, the thin film without ammonolysis and ammonolysis were compared as in the XRD, obtaining the following results (Figure 38):

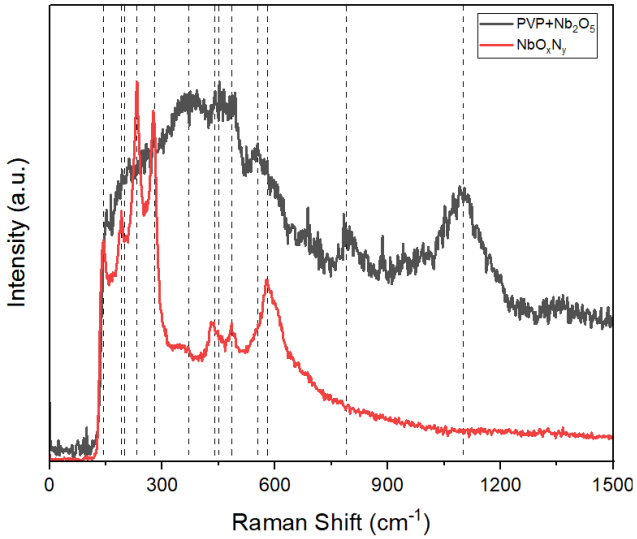

Figure 38: Comparision of Raman spectra of two quartz glass sustrates, one with PvP and Nb_2O_5 (1 mm/s) (black) and the other one with the same characteristics but ammonolyzed (red).

In the ammonolyzed sample, in addition to the higher overall intensity of the spectrum, new or sharper peaks are evident in areas that were previously overlain by the quartz glass signals. New bands below 400 cm^{-1} [stand] out, as well as subtle shifts and broadenings in the 500-700 cm^{-1} region. These additional modes are associated with the formation of niobium oxynitride phases ($NbO_{5-x}N_y$) or else with structural modifications induced by the incorporation of nitrogen into the Nb_2O_5 lattice. Likewise, an increase in the shape of Nb=O stretching modes can be observed (above 900 cm^{-1}), which points to the coexistence of more heterogeneous local environments, typical of partial nitridation. This set of changes agrees with what has been reported in previous studies where treatment in ammonia atmosphere promotes the appearance of new bands associated with oxynitride phases, as well as slight shifts of the characteristic Nb_2O_5 peaks. Overall, the spectrum of the ammonolyzed sample reflects greater structural complexity and the presence of additional vibrational modes, confirming the modification of the Nb_2O_5 layer after the ammonolysis process.

6.3 SEM Results.

6.3.1 SEM of the thin films with silicon substrate

To know the structure of the thin film, the SEM is performed on the samples with different coating speeds, therefore, once the test is performed, the following results are obtained (Figure 39):

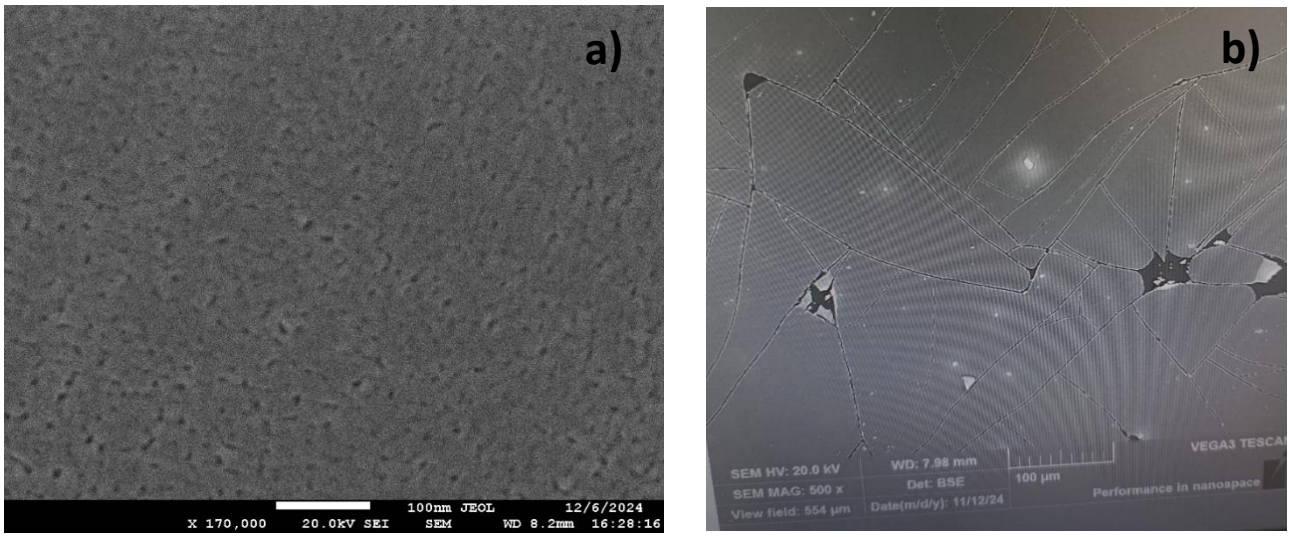

Figure 39: (a) SEM of a withdrawal speed 1 mm/s prepared Nb_2O_5 thin film. (b) SEM of a withdrawal speed of 2 mm/s preapred Nb_2O_5 thin film.

The micrograph shows a coating with a remarkably uniform and porous structure (Figure 39a), with no evidence of cracks when deposited at a rate of 1 mm/s, in contrast to other deposition conditions that did show fractures. The pore size is estimated to be between 15 and 20 nm, suggesting a homogeneous distribution at the nanometer scale. This image allows a clear appreciation of the surface morphology of the coating, showing the continuity and uniformity of the layer, as well as the absence of relevant defects, which is essential for applications requiring high stability and consistent optical or electrical properties.[73]

In contrast (Figure 39b), at deposition rates above 1 mm/s, the thin film tends to crack, probably due to thermo-mechanical stresses produced by thermal expansion of the material at temperatures up to 600 °C. At higher coating speeds, the film may not have enough time to relax and adhere homogeneously, facilitating the formation of cracks. In addition, the very nature of Nb_2O_5, which undergoes phase changes and variations in its crystalline structure at high temperatures, may contribute to defect formation if growth is not properly controlled. These findings highlight the importance of optimizing both deposition rate and process temperature to avoid fractures and ensure stable, functional coatings.[74]

Once the porosity was verified for the oxide thin films before undergoing ammonia treatment, those after ammonolysis were analyzed, obtaining the following results (Figure 40):

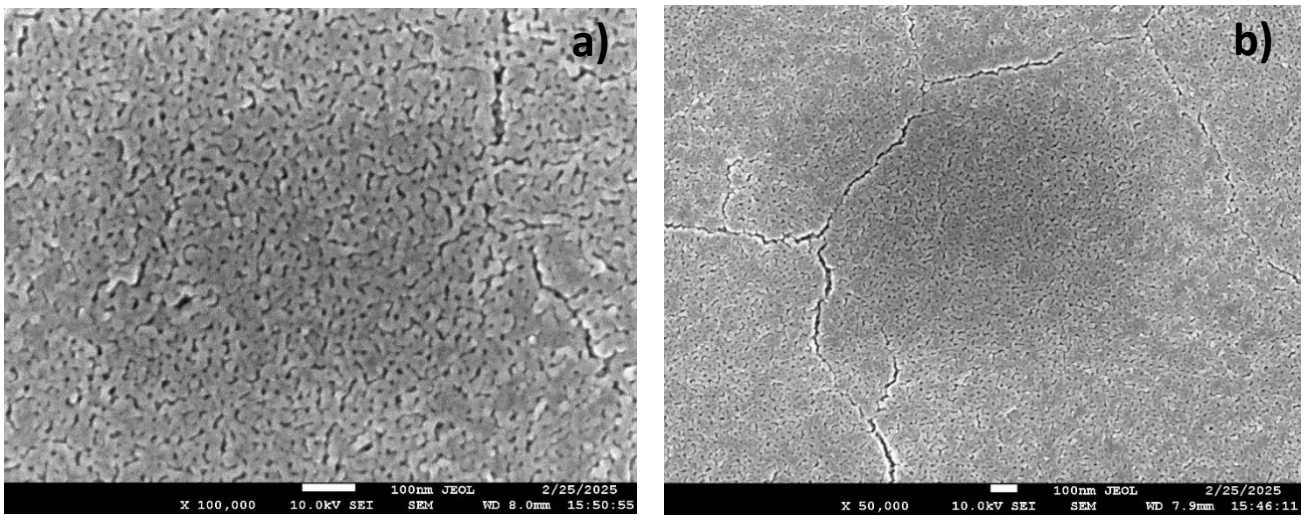

Figure 40: (a) SEM of a withdrawal speed of 1 mm/s prepared Nb_2O_5 ammonolyzed thin film. (b) SEM iamge displaying cracks within the same thin film.

The porous morphology initially observed is preserved, having a pore size around 15-20 nm. However, cracks are observed that could be due to the high thermal regime (800 °C) used during ammonolysis, which generates thermomechanical stresses in the film. However, these fractures are not so significant, since the layer is not completely fragmented, suggesting a possible high activity in PEC experiments since the presence of these pores is vital for the correct functioning of the thin film as an anode.

6.3.2 SEM of the thin films on quartz glass substrate

A thin film of oxynitride ($Nb_2O_{5-x}N_y$) deposited on a quartz glass substrate was also SEM-imaged. During the acquisition of the images, a constant variation in brightness was observed, which prevented to obtain useful images for the adequate characterization of the sample. It is presumed that this fluctuation could be associated with the properties of the quartz glass substrate; however, the influence of other experimental factors is not ruled out.

6.4 UV-Vis results

To be able to see the light absorbing capacity essential for the PEC tests, a previous UV analysis is largely necessary. It is worth mentioning that only ammonolized quartz glass thin films can be measured in this UV-Vis, because Nb_2O_5 thin films are too transparent and silicon substrate thin films totally reflect the light beam used for the measurement. Once the thin films have been tested in their three stages, the following results are obtained (Figure 41):

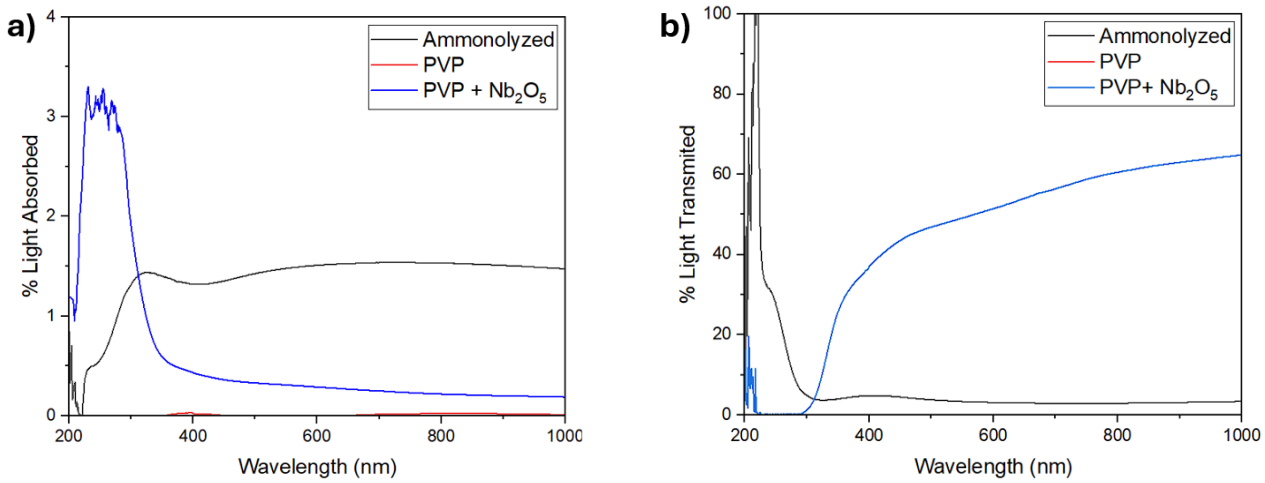

Figure 41: (a) Comparison of the absorbance of the thin film on quartz glass at different stages of its synthesis. (b) Comparison of the transmittance of the same thin films at different stages of its synthesis.

First, the PVP film exhibits very low absorption values over the entire wavelength range analyzed, thus manifesting its high intrinsic transparency. For its part, the PVP + Nb_2O_5 coating exhibits marked absorption in the ultraviolet (UV) region, especially below 350 nm, indicating the presence of the metal oxide which blocks radiation in the UV but retains high transmittance in the visible region. Finally, the ammonolyzed sample retains significant absorption in the UV, but extends slightly into the visible region, reducing the transmittance with respect to the untreated PVP + Nb_2O_5 coating. This change suggests that the ammonolysis process at high temperatures (~800 °C) modifies the structure and the bandgap of Nb_2O_5 by incorporating nitrogen into the crystal lattice. [75]

In the transmission graph, the inverse behavior of each sample can be observed. The pure PVP presents a transmittance close to 100 % in the visible region, while the PVP + Nb_2O_5 coating maintains high transmittance values in the visible, but with a pronounced drop in the UV due to the absorption of the metal oxide. For its part, the ammonolyzed film shows the lowest overall transmittance, consistent with its broader absorption. Even so, it retains a sufficient range of transparency for applications where absorption of UV radiation and part of the visible is required, for example in photocatalysis or photoelectrochemical devices.[75]

From these data, by applying the Tauc Plot method, the optical bandgap of the material can be obtained by regressing it to the following graphs (Figure 42):

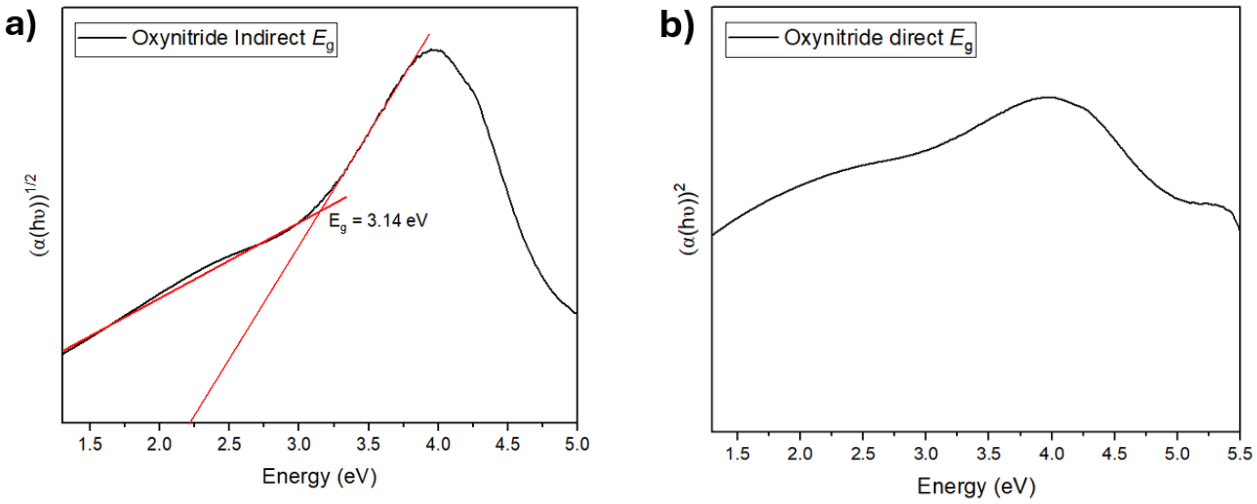

Figure 42: (a) Tauc plot for the indirect bandgap. (b) Tauc Plot for the direct bandgap.

The Tauc Plot method is used to determine the optical bandgap energy (bandgap, E_g) of a material from its absorbance measurements as a function of photon energy. To do this, the wavelength (λ) is converted to energy ($E = hc/\lambda$, expressed in electron volts, eV) and the absorption (α) is obtained experimentally. In the case of direct transitions, $(\alpha h\nu)^2$ versus $h\nu$ (photon energy) is represented, while for indirect transitions $(\alpha h\nu)^{1/2}$ versus $h\nu$ is used.

Therefore, the Tauc equation is defined as:

$$(\alpha h\nu)^n = B\left(h\nu - E_g\right) \quad (9)$$

Where α is the absorption coefficient, $h\nu$ is the photon energy, E_g is the bandgap energy, B is a constant of the equation and n depends on the type of electronic transition (usually n=2 for direct transitions and n=1/2 for indirect ones).

In the plots shown (Figure 42), the absorbance data have been transformed to represent both $(\alpha h\nu)^2$ and $(\alpha h\nu)^{1/2}$. From those curves, tangent lines are extrapolated in the linear region of the plot to find the value of $h\nu$ where the function becomes zero, which is associated with the forbidden band of the material. In this case, the analysis suggests that the indirect transition provides a clearer plot for the extrapolation, obtaining a value of E_g ≈ 3.14 eV. [76]

Such value coincides with what is expected for Nb_2O_5 thin films modified by ammonolysis processes (where nitrogen is incorporated), since it is known that Nb_2O_5 can present a bandgap close to 3.2-3.3 eV, and the addition of nitrogen can cause a slight reduction of this value.

This bandgap reduction suggests an improvement in absorption towards the visible region, which could favor photoelectrochemical or photocatalytic applications, since the material can take advantage of a larger fraction of the solar spectrum.[77]

6.5 XPS results

6.5.1 XPS of an oxide (Nb_2O_5) thin film deposited on silicon

Next, the XPS spectra of an oxide sample deposited on quartz glass is analyzed (Figure 43), these have been measured since they are the ones of strongest interest for the PEC experiments due to their transparency in the UV/Vis part of the solar spectrum, but the type of substrate should not influence the result:

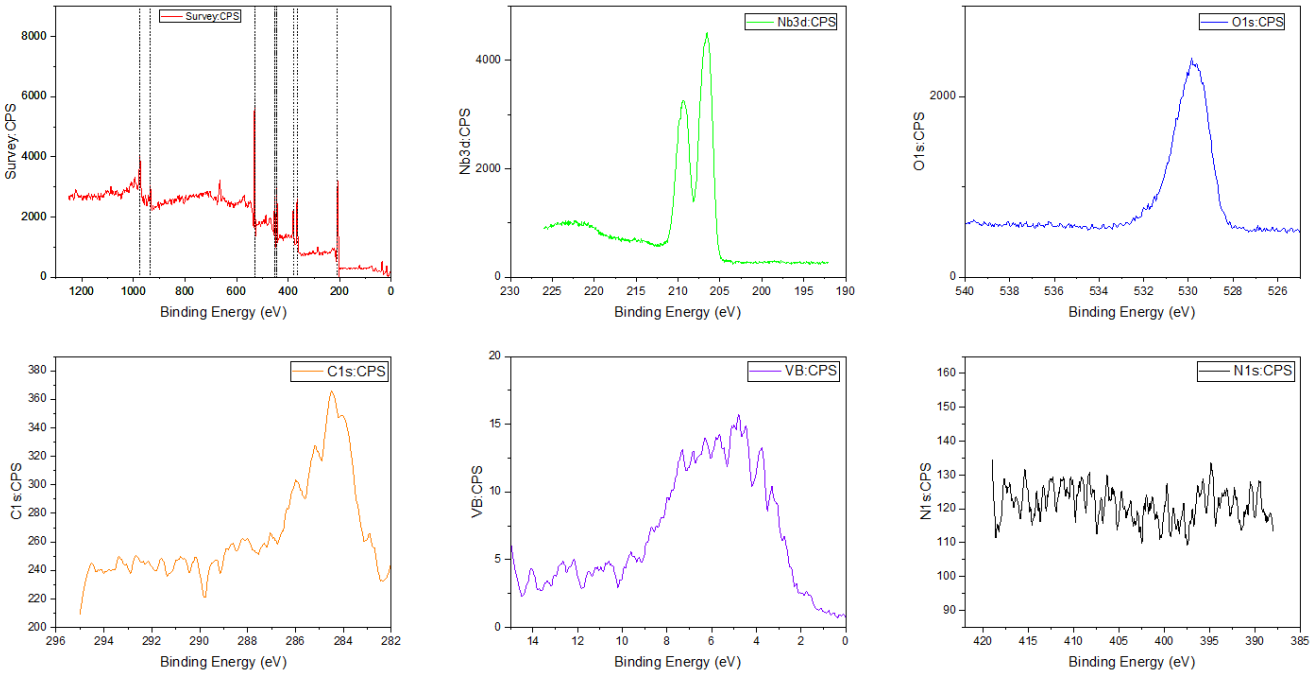

Figure 43: XPS spectra of an oxide thin film.

First, the general scanning analysis (survey) of the XPS spectrum reveals the predominant presence of niobium (Nb) and oxygen (O), along with signals attributable to carbon (C) while the amount of nitrogen (N) can be considered practically absent. The relative intensity of the Nb and O peaks is consistent with the formation of the compound Nb_2O_5, while the carbon signal is interpreted as surface contamination, a common occurrence in samples exposed to the environment.[78]

Two main peaks, located at approximately 207 eV and 210 eV, are seen in the region corresponding to Nb 3d, which are assigned to the Nb $3d_5/_2$ and Nb $3d_3/_2$ core levels, respectively. In the fitting of these components, it was considered that the area of the $3d_5/_2$ and $3d_3/_2$ peaks should have an intensity ratio of 3:2 (due to the spin-orbit splitting degeneracy), and that the position difference between the two peaks should be 2.72 eV

(source: Handbook of XPS). The binding energy of the Nb $3d_5/_2$ peak, located at around 206.6 eV, suggests a Nb^{5+} oxidation state, confirming the presence of Nb_2O_5.[78]

Analysis of the O 1s region reveals a dominant peak located near 530 eV, which is typical of metal-oxygen bonds in metal oxides. A more detailed fit allowed the identification of three components: a peak at 529.5 eV attributed to Nb–O bonds in Nb_2O_5, a component at 530.5 eV related to -OH groups from surface contamination, and a peak at 531.7 eV corresponding to C–O bonds, also arising from surface contamination.[78] This can be seen reflected in figure 44:

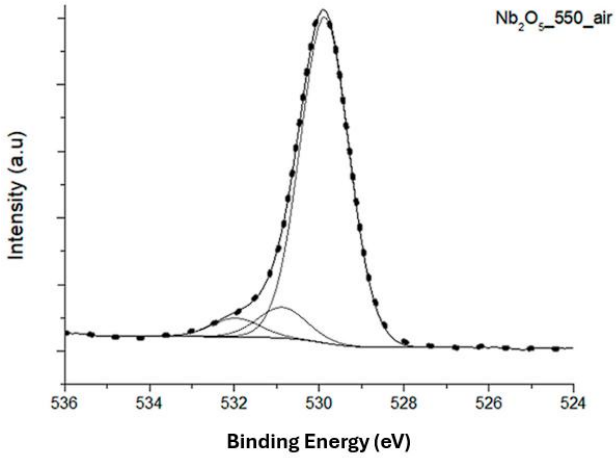

Figure 44: XPS of O1s region of an oxide thin film in detail.[79]

The C 1s region shows a weak peak around 285 eV, associated with C–C and C–H bonds, confirming the presence of organic contaminants adsorbed on the sample surface. This is common in XPS analysis and does not significantly affect the determination of the main oxide composition. Conversely, the signal corresponding to N 1s, around 400 eV, is basically at the noise level, indicating that the concentration of nitrogen in the sample is below the detection limit. This can be easily understood by the high stability of N_2-molecules preventing any reaction between the oxide and the atmosphere at the applied reaction conditions prior to treatment with ammonia.[78]

The valence band spectrum provides complementary information about the electronic structure of Nb_2O_5. It is observed that the valence band edge lies approximately 1.5 to 2 eV below the Fermi level, which is in line with the expected behavior for this type of oxide. This distribution of electronic states supports the characterization of the material as a wide bandgap semiconductor, in agreement with properties reported in the literature.[78]

Finally, quantitative analysis of the areas under the Nb 3d and O 1s peaks indicates an Nb to O ratio close to 2:5, confirming the stoichiometry of Nb_2O_5. The overall results lead to the conclusion that the analyzed thin film is mainly composed of pentavalent niobium and oxygen, with minor levels of surface contaminants, thereby supporting the correct formation of the studied oxide.[78]

6.5.2 XPS of an ammonolyzed thin film deposited on silicon

For a proper comparison, the ammonolyzed thin film (Figure 45) will be compared with the one that has not undergone the ammonia treatment as described in the previous section:

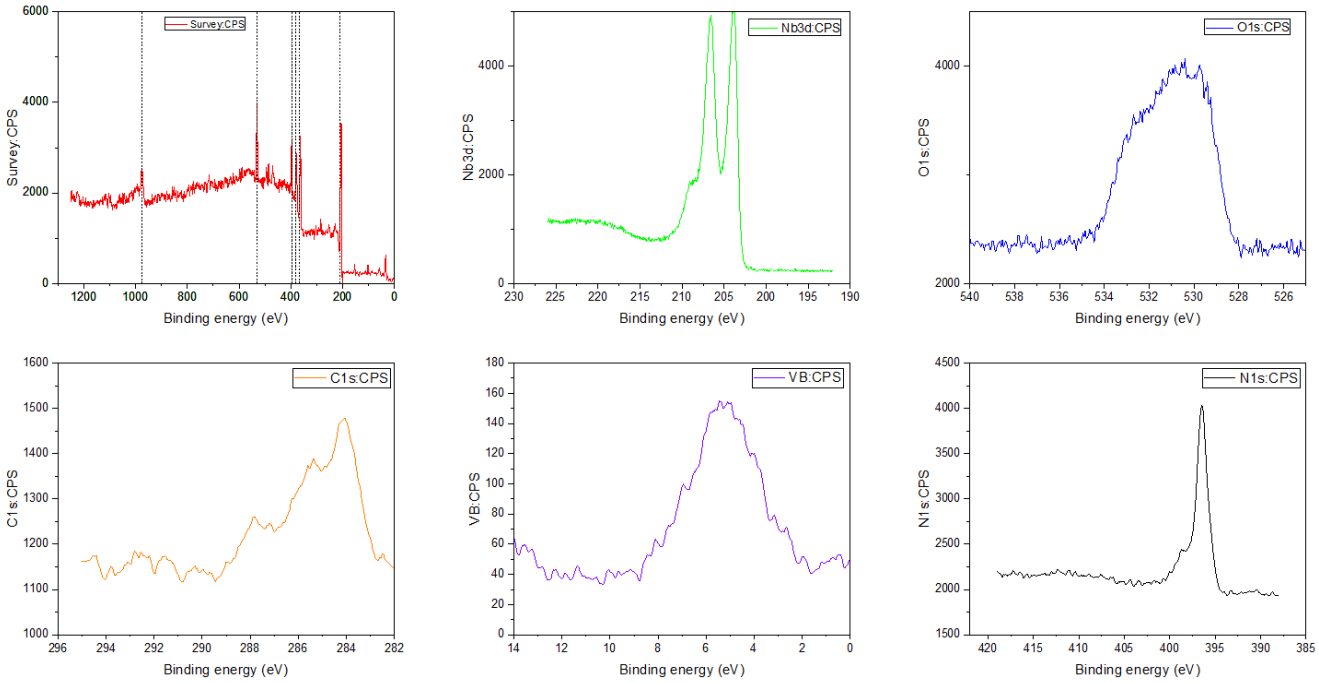

Figure 45: XPS spectra of an ammonolyzed thin film.

When comparing the XPS spectra of both samples, peaks corresponding to niobium (Nb), oxygen (O), and carbon (C) are observed. In the ammonolyzed sample, however, there is a notable increase in the nitrogen (N) signal, suggesting that N has been incorporated either at the surface or within the niobium oxide lattice. The carbon signal is mainly attributed to surface contamination common in samples exposed to the environment, with the peak near 285 eV (associated with C–C, C–H, and related bonds) showing no significant differences between the samples, which indicates that the ammonia treatment does not entirely remove these contaminants.[78]

In both samples, main and sharp Nb $3d_5/_2$ and Nb $3d_3/_2$ peaks (located near 203 eV and 206 eV, respectively) are observed. However, the observed shift of their binding energy implies the presence of niobium cations in a lower oxidation state. Additionally, an extra “bump” at a higher binding energy of 210 eV characteristic of Nb in the +5 oxidation state (Nb_2O_5). In the ammonolyzed sample, although no significant overall shift in the binding

energy is observed, the peaks exhibit a slight broadening. To further elucidate the chemical situation a fitting was applied to the peaks. For the Nb 3d region, four components were fitted. The fitting included the same two components corresponding to Nb_2O_5 as before, along with two additional components associated with a more reduced niobium oxidation state (most likely Nb^{3+} from NbN). These components were fitted with the same constraints as before, with the area ratio between Nb $3d_5/_2$ and Nb $3d_3/_2$ maintained at 3:2 for the Nb_2O_5 peaks. The full width at half maximum (FWHM) of the Nb^{3+} components was chosen to be broader, acknowledging that the ammonolysis process may introduce further oxidation states, bond changes, or chemical contributions that result in small additional peaks not plotted due to their minimal contributions. The ratio of Nb species was concluded to be approximately 64% Nb^{3+} to 36% Nb^{5+}.[78] This observation is in line with literature reports on 800 °C ammonolysis, leading to the formation of mixed phases and even compounds closer to NbN.[78]

The main O 1s peak, located around 530 eV, remains dominant in both samples, confirming the prevalent presence of metal-oxygen bonds. In the ammonolyzed sample, additional contributions in the O 1s region are attributed to nitrates and Nb–O bonds with different neighboring interactions depending on the surrounding surface. However, it is difficult to quantify these contributions precisely. A subtle change in the relative intensity of the O 1s peak may also indicate a partial substitution of oxygen by nitrogen in the lattice, along with a small contribution at higher binding energies likely associated with hydroxyl (-OH) groups or adsorbed water. This feature is more pronounced compared to the oxide, possibly due to the addition of hydrogen to the surface during ammonolysis.[78]

The N 1s region displays three distinct components in the ammonolyzed sample. These components are identified at approximately 396.4 eV (attributed to NbN), 398.6 eV (possibly associated with NH_3), and 400 eV (which could correspond to N-organic species). In the oxide precursor, the N signal is almost residual, whereas in the ammonolyzed sample it increases significantly, supporting the incorporation of nitrogen either as Nb–N bonds or as adsorbed species on the surface.[78]

The fundamental valence band spectra still display the electronic state distribution characteristic of Nb_2O_5. However, in the ammonolyzed sample, slight variations are observed. These changes are likely to be due to the introduction of nitrogen and the consequent formation of NbN which exhibits a metallic electronic structure.[78]

Finally, the Nb/O ratio in both samples remains close to 2:5, confirming that Nb_2O_5 is the predominant oxide phase. However, after ammonolysis, additional Si peaks are visible from the substrate, suggesting possible degradation of the thin film during the ammonia treatment. Taken together, these results show that ammonia treatment promotes nitrogen incorporation in the thin film surface, generating slight changes in the Nb 3d and O 1s spectral regions, and a clear increase in the N 1s intensity, without drastically modifying the main

pentavalent niobium phase. This evidence confirms the effective formation of nitride or partially oxynitride niobium species after the ammonolysis process.[78]

6.5.3 XPS of an ammonolyzed thin film deposited on quartz glass after PEC test

Finally, an ammonolyzed sample after the PEC experiments (analyzed later) is compared (Figure 46) with the sample before undergoing the test:

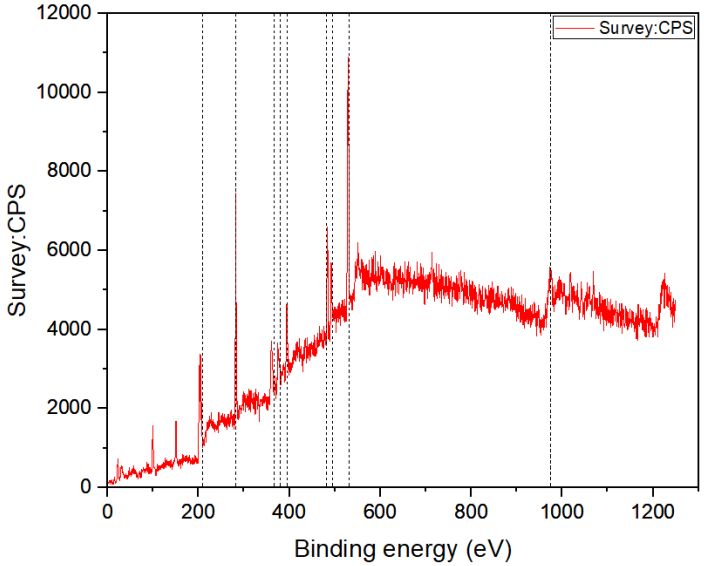

Figure 46: XPS spectra of an oxynitride $Nb_2O_{5-x}N_y$ thin film after PEC test.

After the PEC experiment, the XPS survey spectrum shows significant charging, indicating that the sample is no longer conductive hampering a detailed analysis of the core level spectra. After correcting the spectrum with the flood gun for electron compensation, signals for niobium (Nb) and nitrogen (N) are still visible; however, there is a marked increase in oxygen (O) and carbon (C) signals. These enhanced O and C peaks are attributed to surface contamination from the electrolyte or residual intermediates of the electrochemical reactions.

Additionally, the spectrum reveals a stronger signal from the silicon (Si) substrate, which suggests that the thin film may have corroded or detached during the PEC process. Due to the high charging effects, further detailed evaluation of the XPS data is not possible in this case.

6.6 PEC results

6.6.1 PEC results of the oxide (Nb_2O_5) thin film deposited on silicon

The results of the PEC measurement of a Nb_2O_5 (oxide) thin film deposited on silicon under UV irradiation (500 W/m²) and under visible illumination (1000 W/m²) are presented (Figure 47):

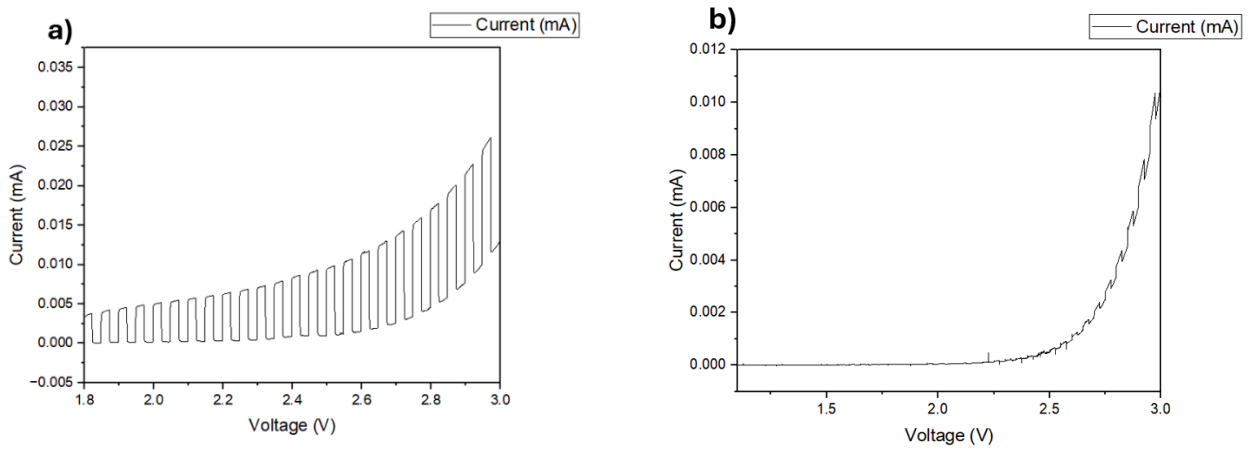

Figure 47: PEC results on silicon substrate oxide thin film with a UV lamp (500 W/m²) (a). PEC results of the same thin film with visible light (1000 W/m²) (b).

Under UV irradiation, the photogenerated current reaches approximately 2.5×10^{-5} A over the range of potentials studied, indicating a higher photoelectrochemical activity in the ultraviolet region. This behavior confirms that, despite the limitations inherent to Nb_2O_5 (namely, its broad band gap that restricts visible light absorption) the charge separation process is better optimized under UV light. Specifically, under 500 W/m² UV irradiation, the Nb_2O_5 film responds more efficiently to high-energy photons, facilitating the absorption of ultraviolet light and the generation of electron-hole pairs. Additionally, the observed "steps" or periodic fluctuations in the current curve are not a result of charge traps or defects; rather, they arise from the measurement protocol, where the illumination is cycled on and off every 10 seconds.

In contrast, under visible illumination the peak current is about 1.2×10^{-5} A, confirming that the PEC response in this region is lower, even when higher light intensity (1000 W/m²) is used.

These results suggest that additional treatments (such as ammonolysis to add nitrogen) will be necessary to shift the absorption threshold toward the visible and improve charge separation efficiency.

6.6.2 PEC results of the oxynitride ($Nb_2O_{5-x}N_y$) thin film deposited on silicon

Initially, the photogenerated current versus applied voltage curves are measured under two illumination conditions, ultraviolet (500 W) and visible light (1 kW, simulating the solar spectrum) (Figure 48):

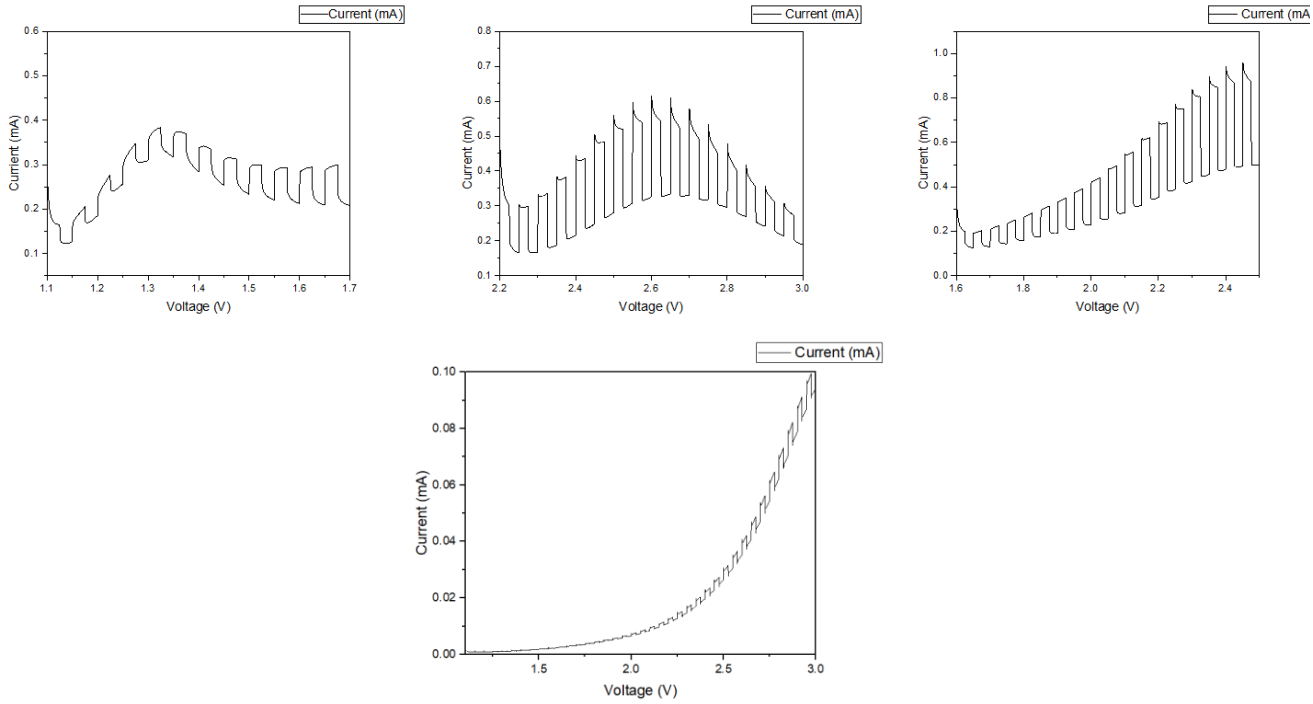

Figure 48: At the top, PEC results on silicon substrate thin film ammonolyzed at 800ºC with a UV lamp (500 W/m^2), at the bottom PEC results of the same thin film with visible light (1000 W/m^2).

Under 500 W/m^2 UV irradiation (It is worth mentioning that if alienated graphs appear, it means that the same experiment has been performed but with different voltages), the photoinduced current reaches approximately 0.001 A, evidencing that the $Nb_2O_{5-x}N_y$ film responds more efficiently to high-energy photons. This is consistent with the relatively large band gap of the material, which facilitates the absorption of ultraviolet light and the generation of electron-hole pairs. Also note that the peaks that appear at the beginning of the illumination on the PEC is an indication of charge trapping and it is not present for Nb_2O_5.

In contrast, measurements made with the 1 kW visible light source show much lower currents, around 0.0001 A. Despite the higher lamp power, the lower photon energy in the visible range hinders the excitation of electrons across the forbidden band of $Nb_2O_{5-x}N_y$, significantly reducing the generated carrier density. This limitation may be aggravated by the existence of defects or intermediate states that favor recombination of electron-hole pairs when the carrier density is low.

Comparison of the peak currents (0.001 A in UV vs. 0.0001 A in visible) reveals a notably higher photoelectrochemical response under ultraviolet irradiation, confirming the suitability of the oxynitride for applications where high-energy photons are available. Although ammonolysis can modify the structure of Nb_2O_5 to some extent, it is not sufficient to achieve similar performance in the visible region. Consequently, if more effective harnessing of solar radiation is desired, it will be necessary to resort to doping strategies or coupling with other materials that extend their absorption window toward longer wavelengths.

Therefore, the results demonstrate that the oxynitride film on silicon substrate operates particularly efficiently under ultraviolet irradiation, achieving photoinduced currents of higher magnitude than under visible light. This finding evidences the potential of Nb_2O_5 in high photon energy regions, it is also worth noting that this niobium oxynitride thin film is an N-type semi-conductor, because the higher the voltage the higher the activity, i.e., it is anodic.

To determine whether the temperature of ammonolysis affects the results, the same experiment is performed but with a thin film that has undergone ammonia treatment at 750 ºC (Figure 49):

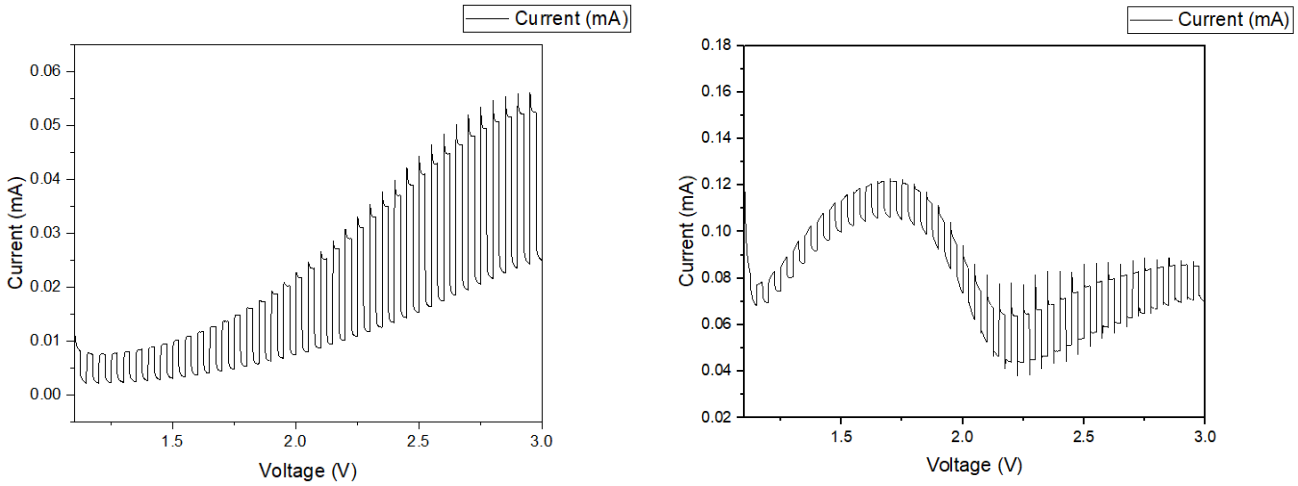

Figure 49: On the left, PEC results on silicon substrate thin film ammonolyzed at 750ºC with a UV lamp (500 W/m^2), on the right PEC results of the same thin film with visible light (1000 W/m^2).

In the curve on the left (500 W/m^2), the photoinduced current increases progressively with voltage until it reaches a value close to 6 × 10^{-5} A. A staggered pattern is seen due to the periodic switching on and off the light source, which generates regular oscillations. The shape of the curve suggests a gradual accumulation of photogenerated carriers, with stepwise increases that stabilize as a higher voltage is reached.

On the other hand, in the curve on the right (1 kW/m^2), the current intensity is somewhat higher, reaching approximately 1 × 10^{-4} A. Although radiation in the visible region is not always the most effective for Nb_2O_5 (due to its relatively large band gap), in this case the total light power is higher and seems to favor slightly higher carrier generation.

As for direct comparison, it is observed that the 1 kW/m^2 curve is more intense than the 500 W curve, around twice the maximum current recorded. This difference can be attributed both to the higher power of the source and to possible structural and electronic changes in the film due to the ammonolysis process at 750 °C, which could allow a slightly extended absorption or a better carrier separation in the visible light range.

In conclusion, for these samples treated at 750 °C, more intense photoelectrochemical behavior is evident under 1 kW illumination than under 500 W illumination, although with somewhat different response patterns in terms of curve shape. This suggests that, even with $Nb_2O_{5-x}N_y$ being more tunable to the ultraviolet range, increased light power and variations in the ammonolysis process may favor a higher photoinduced current under visible light.

In general, measurements suggest that ammonolysis at 800 °C gives a higher response under ultraviolet irradiation (with currents on the order of 1×10^{-3} A), compared to films treated at 750 °C (hovering around 6×10^{-6} A in UV). However, in the visible region, the difference between the two treatment temperatures is not as pronounced (around 1×10^{-4} A). Therefore, if the main objective is to optimize activity under UV light, the 800 °C temperature appears more suitable. For visible light-oriented applications, the benefit of increasing the temperature to 800 °C is less evident. It is also important to note that the measurements were performed in a neutral pH electrolyte, which closely resembles water and is one of the most challenging conditions to achieve high photoelectrochemical performance. The fact that a response was obtained under these conditions is promising, and exploring other electrolytes could potentially enhance the results.

6.6.3 PEC results of the oxynitride ($Nb_2O_{5-x}N_y$) thin film deposited on quartz glass

First, the oxynitride film on quartz glass substrate was analyzed. In this case, not clearly defined photoelectrocatalytic behavior was observed. Despite irradiation with lamps of different power (500 W/m^2 in the ultraviolet range and 1 kW/m^2 in the visible), the photoinduced current response was practically null or very small, indicating that the quartz glass substrate, combined with the ammonolysis conditions, did not provide the appropriate conductivity or electronic configuration to generate significant photoinduced currents.

Furthermore, when the ammonolyzed film was treated at 800 °C on quartz glass, a loss of conductivity was detected prior to the PEC tests, resulting in a current response close to zero. This suggests that excessive heat treatment or the formation of secondary phases may impair the crystal structure and conductivity of Nb_2O_5 on quartz glass, thus preventing efficient charge carrier transport. This observation aligns with the XRD, Raman, and XPS results, which indicate that the material obtained after ammonolysis on silicon and quartz glass substrates may exhibit chemical differences. Such variations in composition and structure inevitably impact the PEC performance, as the properties of the material are not identical on both substrates.

A general analysis of the PEC results of the $Nb_2O_{5-x}N_y$ thin film at 750 °C under two different illumination conditions follows. It should be noted that unlike the one ammonolyzed at 800 °C, the one at 750 °C does retain some resistivity, around 2.9 Ω) (Figure 50):

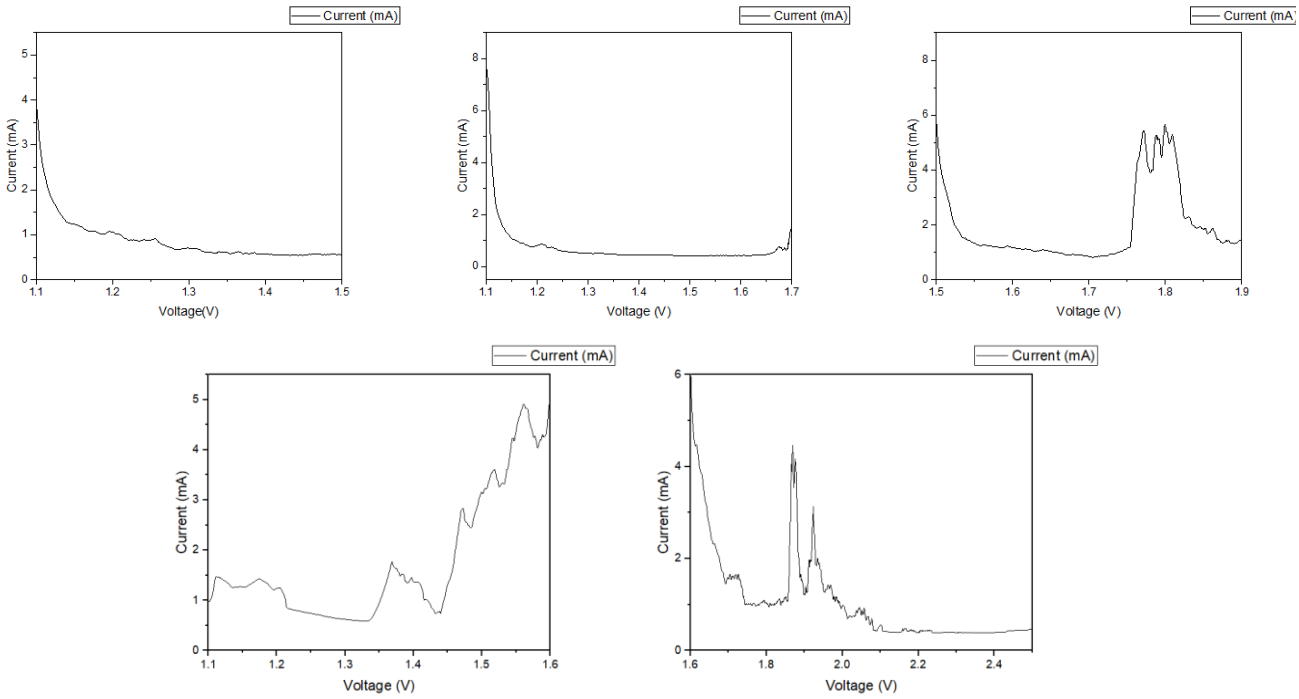

Figure 50: At the top, PEC results on quartz glass substrate thin film ammonolyzed at 750ºC with a UV lamp (500 W/m^2), at the bottom PEC results of the same thin film with visible light (1000 W/m^2).

Under irradiation with a 500 W/m^2 UV lamp, a response was obtained in which the photoinduced current remained at very low values and showed an almost irregular evolution as the applied potential was increased. This result indicates that, under these conditions, electron-hole pair generation is limited, and charge separation is inefficient, resulting in poor photoelectrochemical activation.

On the other hand, when the same sample was irradiated with a 1 kW/m^2 visible light lamp, a very weak current response was again observed. The corresponding graph reveals that, despite the higher light power, the photoinduced current remains minimal, exhibiting no noticeable peaks or steps. This is primarily attributed to the wide band gap of $Nb_2O_{5-x}N_y$, which hinders the excitation of electrons with lower energy photons present in the visible range, which, in turn, affects the carrier density generated.

These results suggest that the interaction between the film and the quartz glass substrate leads to the formation of a mixed-phase material, including Nb_2O_5, NbO, and NbN, as indicated by the XPS analysis. The presence of reduced Nb species and free carriers (electrons) may hinder charge separation efficiency, which is reflected in the negligible photoelectrochemical response across both spectral ranges. In contrast, in experiments performed with a silicon substrate, a much more pronounced response was achieved, highlighting

the influence of material composition on PEC performance. To mitigate this effect, an alternative approach could involve using an electrolyte capable of absorbing excess charge carriers, as previously suggested.

In conclusion, the Nb_2O_5 film ammonolyzed at 750 °C on quartz glass substrate shows poor photoelectrochemical behavior both under UV irradiation and in the visible range. The low activity recorded is due to the limited generation of electron-hole pairs and inefficient charge separation, which contrasts markedly with the behavior observed in samples deposited on silicon substrate, where a higher efficiency in the photoelectrocatalytic response is achieved.

Finally, trying to obtain some results in other experiments, we proceeded to use this thin film in the cathodic region in ultraviolet light (500 W/m^2) (i.e., decreasing the voltage gradually) obtaining the following results (Figure 51):

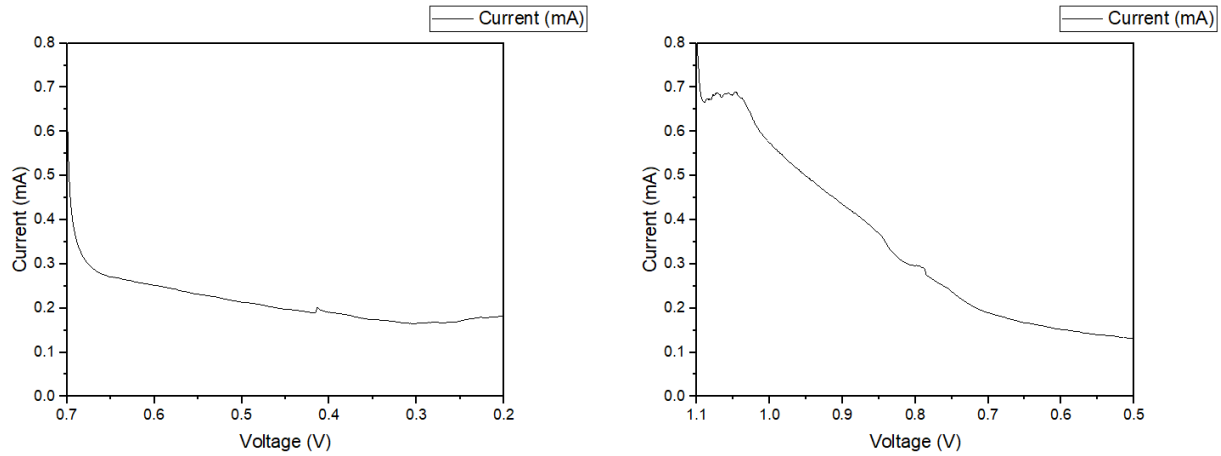

Figure 51: PEC on quartz glass substrate ammonolyzed at 750ºC with a UV lamp (500 W/m^2) in the cathodic region.

Negative voltages were applied to explore possible photoinduced reactions and to evaluate if the material could show any photoactivity behavior under cathodic conditions. The obtained plots reveal that the measured current remains at very low value and does not show significant increases under illumination, indicating the absence of relevant photoelectrochemical activity in this potential range.

The lack of response in the cathodic region confirms the limited ability of oxynitrides to generate and separate charge carriers when operating under reducing conditions on quartz glass substrates.

These findings, coupled with the absence of photoinduced current in the cathodic region, reinforce the conclusion that Nb_2O_5 ammonolyzed at 750 °C with quartz glass substrates is not suitable for most PEC experiments seeking high efficiency in the generation of oxidation or reduction products. Although ammonolysis can modify certain electronic properties of niobium oxide, the necessary adjustments to extend activity significantly into the cathodic region or for photon absorption in the visible range have not been achieved.

In conclusion, this thin film does not exhibit significant photoelectrocatalytic activity under cathodic conditions, which aligns with the initial objective of developing an n-type semiconductor. The absence of a satisfactory response across the visible spectrum and cathodic potential range indicates that, in its current form, $Nb_2O_{5-x}N_y$ at 750 °C does not meet the requirements for an efficient photoelectrochemical device. This highlights the need to explore alternative doping strategies, structural modifications, or combinations with other semiconductors to enhance its performance.

7 Summary

Nb_2O_5 thin films were synthesized by the dip-coating method on silicon and quartz glass substrates. The precursor solution was prepared by dissolving $NbCl_5$ in ethanol with the assistance of Pluronic F-127 and citric acid, ensuring a homogeneous mixture for the coating process. The substrates underwent an extensive cleaning protocol (including treatments with ethanol, acetone, sonication, and ozone cleaning) to guarantee optimal adhesion of the deposited film. After deposition, the films were dried at 125 °C and subsequently calcined at 600 °C in air, which induced the crystallization of Nb_2O_5 with a pseudohexagonal structure.

Following calcination, the films were subjected to ammonolysis at temperatures of 750 °C and 800 °C under a flowing ammonia atmosphere for 3 hours. This process promoted nitrogen incorporation into the films, leading to the formation of mixed phases (NbN, Nb_2O_5 and possible oxynitride phases) and a partial reduction of niobium from the +5 to a lower oxidation state (approximately a 64% Nb^{3+} to 36% Nb^{5+} ratio). Structural analysis by X-ray diffraction (XRD) confirmed the formation of pseudohexagonal Nb_2O_5, while Raman spectroscopy evidenced the presence of characteristic Nb–O and Nb=O vibrational modes. Moreover, after ammonolysis, new bands appeared at lower energy (below 400 cm^{-1}), indicating the formation of Nb–O–N bonds and the coexistence of oxynitride or nitride phases.

X-ray photoelectron spectroscopy (XPS) provided further insight into the chemical composition. In ammonolyzed samples, nitrogen was successfully incorporated, and mixed niobium oxidation states were observed, supporting the partial transformation toward Nb–N species. However, post-PEC (photoelectrochemical) testing, the XPS survey indicated strong charging effects, with the sample losing its conductivity. The corrected spectra revealed an increase in oxygen and carbon signals—attributed to contamination from the electrolyte or residual reaction intermediates—and a more pronounced presence of silicon from the substrate, suggesting that the thin film suffered degradation or partial detachment during PEC operation.

PEC performance tests under UV (500 W/m^2) and visible (1000 W/m^2) illumination showed that films ammonolyzed at 800 °C on silicon substrates exhibited significantly enhanced photocurrent under UV light (approximately 1 mA), indicating improved charge separation. In contrast, the response under visible light remained low (around 100 µA), and films on quartz glass demonstrated minimal PEC activity, likely due to less efficient charge carrier transport across the interface. Furthermore, the post-PEC degradation and charging effects highlight a challenge in the chemical stability of the films under operating conditions. It is also worth mentioning that an applied bias was used during the measurements, which is relevant to the interpretation of the results.

In summary, while ammonolysis at 800 °C improves the UV-driven PEC performance of Nb_2O_5 films by partially reducing the bandgap and incorporating nitrogen, it does not sufficiently extend visible light absorption. Additionally, the observed degradation and loss of conductivity after PEC testing indicate that further optimization (such as enhanced stabilization, doping, or the formation of heterostructures) is necessary to achieve long-term durability and broader spectral activity in photoelectrochemical applications.

8 Outlook/Future work

This work has demonstrated the viability of ammonolysis for modifying Nb_2O_5 and enhancing its photoelectrochemical activity. However, several aspects remain to be addressed in future research to optimize both the performance and stability of thin films. In this regard, it is crucial to delve deeper into optimizing the quartz glass substrate, since the PEC tests yielded unsatisfactory results. Investigating pre-treatment or surface functionalization techniques for quartz glass could lead to better adhesion and improved charge transfer between the substrate and the deposited film.

Another important aspect to consider is the improvement of operating conditions at 800 °C. Although this treatment promotes the formation of desirable phases, it has been observed that conductivity may be compromised, also the indicated formation of NbN in the XPS suggests that the ammonolysis conditions at 800 °C are already too aggressive. Therefore, it is recommended to explore adjustments in parameters such as ammonia flow rate, treatment duration, and the implementation of more controlled heating ramps, with the aim of preserving conductivity without sacrificing adequate nitrogen incorporation.

Furthermore, the quality and uniformity of thin films depend greatly on the composition of the precursor solution. This can be studied by varying the concentrations of $NbCl_5$, Pluronic F-127, and citric acid (as well as the solvent proportions) should be carried out to establish the optimal conditions that yield more homogeneous films with structural characteristics ideal for efficient charge transfer.

In addition, the incorporation of dopants or the formation of heterostructures represents a promising avenue to broaden the absorption spectrum into the visible range and reduce carrier recombination. Combining Nb_2O_5 with other semiconductors or introducing transition metals could significantly enhance photoelectrochemical efficiency. Alongside this, the integration of co-catalysts, such as Pt, RuO_2, or more abundant material alternatives, may facilitate oxygen evolution and water reduction, thus improving the overall system performance without considerably increasing costs.

In order to strengthen the scientific understanding of the substrate-film-interface by advanced electrochemical characterization and further evaluation of the effects caused by the electrical bias are necessary. Finally, it is crucial to assess the stability and durability of the films under real operational conditions. Long-term PEC studies are recommended to analyze the evolution of the surface composition and to detect any reoxidation or nitrogen loss, employing in situ techniques such as XPS or Raman spectroscopy. Complementing the experimental approach with theoretical modeling and simulations that address defect distribution, internal stresses, and phase evolution during thermal treatment and ammonolysis will be essential for a deeper understanding of the underlying mechanisms and for guiding future process optimizations.

Collectively, these proposals for future work will not only contribute to optimizing the efficiency of Nb_2O_5 based photoelectrochemical cells but will also expand the knowledge on how synthetic and treatment parameters affect the stability and performance of semiconductor materials for solar energy conversion applications.

9 References

1. Van de Krol, R. & Gratzel, M. Photoelectro-Chemical Hydrogen Production Roel van de Krol Michael Grätzel. http://www.springer.com/series/5915. (last access 26/03/2025)

2. Mauna Loa Observatory - NOAA Global Monitoring Laboratory. https://gml.noaa.gov/obop/mlo/.(last access 26/03/2025)

3. Gao, J., Yao, T., Masson-Delmotte, V., Steen-Larsen, H. C. & Wang, W. Collapsing glaciers threaten Asia's water supplies. Nature 2021 565, 19–21 (2019).

4. Pacto Verde Europeo - Consilium. https://www.consilium.europa.eu/es/policies/green-deal/. (last access 26/03/2025)

5. The Future of Hydrogen – Analysis - IEA. https://www.iea.org/reports/the-future-of-hydrogen. (last access 26/03/2025)

6. Villa, K., Galán-Mascarós, J. R., López, N. & Palomares, E. Photocatalytic water splitting: advantages and challenges. Sustainable Energy and Fuels vol. 5 4560–4569 Preprint at https://doi.org/10.1039/d1se00808k (2021).

7. Jafari, T. et al. Photocatalytic water splitting - The untamed dream: A review of recent advances. Molecules vol. 21 (7), 900. Preprint at https://doi.org/10.3390/molecules21070900 (2016).

8. Osterloh, F. E. & Parkinson, B. A. Recent developments in solar water-splitting photocatalysis. MRS Bull 36, 17–22 (2011).

9. Maeda, K. Photocatalytic water splitting using semiconductor particles: History and recent developments. Journal of Photochemistry and Photobiology C: Photochemistry Reviews 12, 237–268 (2011).

10. Jiang, C., Moniz, S. J. A., Wang, A., Zhang, T. & Tang, J. Photoelectrochemical devices for solar water splitting-materials and challenges. Chemical Society Reviews vol. 46 4645–4660 Preprint at https://doi.org/10.1039/c6cs00306k (2017).

11. Kumar, M., Meena, B., Subramanyam, P., Suryakala, D. & Subrahmanyam, C. Recent trends in photoelectrochemical water splitting: the role of cocatalysts. Article number: 88. NPG Asia Mater 14, (2022).

12. Wagner, A., Sahm, C. D. & Reisner, E. Towards molecular understanding of local chemical environment effects in electro- and photocatalytic CO_2 reduction. Nature Catalysis vol. 3 775–786 Preprint at https://doi.org/10.1038/s41929-020-00512-x (2020).

13. Liao, P. & Carter, E. A. New concepts and modeling strategies to design and evaluate photo-electro-catalysts based on transition metal oxides. Chem Soc Rev 42, 2401–2422 (2013).

14. Bhattacharjee, J. & Roy, S. Synergistic insights: electro-organic photocatalysis and nanostructures. Chemical Papers Preprint at https://doi.org/10.1007/s11696-024-03657-2 (2024).

15. Lohaus, C., Klein, A. & Jaegermann, W. Limitation of Fermi level shifts by polaron defect states in hematite photoelectrodes. Nature Communications 2018 9:1 9, 1–7 (2018).

16. Zhao, Y., Zhou, S. & Zhao, J. Selective C-C Coupling by Spatially Confined Dimeric Metal Centers. (2020). Volume 23, Issue 5, 22 May 2020, 101051

17. Brinker, C. J., Lu, Y., Sellinger, A. & Fan, H. Evaporation-Induced Self-Assembly: Nanostructures Made Easy**. Adv. Mater. 1999, 11, No. 7 doi:10.1002/(SICI)1521-4095(199905)11:7.

18. Yin, J. et al. Light absorption enhancement by embedding submicron scattering TiO_2 nanoparticles in perovskite solar cells. RSC Adv 6, 24596–24602 (2016).

19. Einert, M. et al. Mesoporous $CuFe_2O_4$ Photoanodes for Solar Water Oxidation: Impact of Surface Morphology on the Photoelectrochemical Properties**. Chemistry – A European Journal 29, e202300277 (2023).

20. Kirchberg, K., Wang, S., Wang, L. & Marschall, R. Mesoporous $ZnFe_2O_4$ Photoanodes with Template-Tailored Mesopores and Temperature-Dependent Photocurrents. ChemPhysChem 19, 2313–2320 (2018).

21. Sivula, K., Le Formal, F. & Grätzel, M. Solar water splitting: progress using hematite (α-Fe_2O_3) photoelectrodes. ChemSusChem 4, 432–449 (2011).

22. Fuertes, A. Chemistry and applications of oxynitride perovskites. J Mater Chem 22, 3293–3299 (2012).

23. Breckenridge, M. H. et al. High n -type conductivity and carrier concentration in Si-implanted homoepitaxial AlN. Appl Phys Lett 118, 112104 (2021).

24. Ebbinghaus, S. G., Aguiar, R., Weidenkaff, A., Gsell, S. & Reller, A. Topotactical growth of thick perovskite oxynitride layers by nitridation of single crystalline oxides. Solid State Sci 10, 709–716 (2008).

25. Aguiar, R. et al. The vast colour spectrum of ternary metal oxynitride pigments. Dyes and Pigments 76, 70–75 (2008).

26. Lee, J. S. Photocatalytic water splitting under visible light with particulate semiconductor catalysts. Catalysis Surveys from Asia 9, 217–227 (2005).

27. Kawashima, K. et al. NH3-Assisted Flux-Mediated Direct Growth of $LaTiO_2N$ Crystallites for Visible-Light-Induced Water Splitting. Journal of Physical Chemistry C 119, 15896–15904 (2015).

28. Oehler, F., Naumann, R., Köferstein, R., Hesse, D. & Ebbinghaus, S. G. Photocatalytic activity of $CaTaO_2N$ nanocrystals obtained from a hydrothermally synthesized oxide precursor. Mater Res Bull 73, 276–283 (2016).

29. El-Shazly, T. S., Hassan, W. M., Abd El Rehim, S. S. & Allam, N. K. Optical and electronic properties of niobium oxynitrides with various N/O ratios: insights from first-principles calculations. J Photonics Energy 8, 1 (2018).

30. Honig, J. M., Sinha, A. P. B., Wahnsiedler, W. E. & Kuwamoto, H. Studies of the Band Structure of NbO by X-Ray Photoelectro Spectroscopy. physica status solidi (b) 73, 651–654 (1976).

31. Sudhir Ekande, O. & Kumar, M. Self-powered piezoelectric $NaNbO_3$ induced band position rearrangement and electrocatalysis in MoS_2/$NaNbO_3$ heterojunction for generation of reactive oxygen species for organic pollutant removal. Chemical Engineering Journal 458, 141454 (2023).

32. Dip Coating: Practical Guide to Theory and Troubleshooting | Ossila. https://www.ossila.com/pages/dip-coating. (last access 26/03/2025)

33. Dip Coating Companies | Dip Coating Services. https://dipmoldedplastics.com/dip-coating/.

34. Kościelska, B. & Winiarski, A. Structural investigations of nitrided Nb_2O_5 and Nb_2O_5–SiO_2 sol–gel derived films. J Non Cryst Solids 354, 4349–4353 (2008).

35. Wang, X. J. et al. Niobium(V) Oxynitride: Synthesis, Characterization, and Feasibility as Anode Material for Rechargeable Lithium-Ion Batteries. Chemistry – A European Journal 18, 5970–5978 (2012).

36. Orlov, V. M. & Osaulenko, R. N. Properties of Nitrides Prepared by the Ammonolysis of Magnesiothermic Niobium Powders. Inorganic Materials Vol 54, 639–644, (2018)

37. Epp, J. X-ray diffraction (XRD) techniques for materials characterization. Materials Characterization Using Nondestructive Evaluation (NDE) Methods 81–124 (2016) doi:10.1016/B978-0-08-100040-3.00004-3.

38. Braeuer, A. Raman Spectroscopy From an Engineering Point of View. Supercritical Fluid Science and Technology 7, 193–281 (2015).

39. Ali, A., Zhang, N. & Santos, R. M. Mineral Characterization Using Scanning Electron Microscopy (SEM): A Review of the Fundamentals, Advancements, and Research Directions. Applied Sciences 2023, Vol. 13, Page 12600 13, 12600 (2023).

40. Pavia, D. L., Lampman, G. M., Kriz, G. S. & Vyvyan, J. R. INTRODUCTION TO SPECTROSCOPY. Thomson learning, (2013), vol 3rd.

41. Hollas, J. Michael. Modern spectroscopy. British Library Cataloguing in Publication Data. 2013. Vol 4th.

42. Briggs, D., Seah, M. P. & Wiley, J. Practical surface analysis by Auger and X-ray photoelectron spectroscopy. D. Briggs and M. P. Seah (Editors). John Wiley and Sons Ltd, Chichester, 1983, 533 pp. Surface and Interface Analysis 6, 302–302 (1984).

43. Watts, J. F. & Wolstenholme, J. An Introduction to Surface Analysis by XPS and AES. An Introduction to Surface Analysis by XPS and AES (2003) doi:10.1002/0470867930.

44. Gallenberger, J. et al. Stability and decomposition pathways of the NiOOH OER active phase of NiO_x electrocatalysts at open circuit potential traced by ex situ and in situ spectroscopies. Catal Sci Technol 13, 4693–4700 (2023).

45. ICSD -. https://icsd.fiz-karlsruhe.de/index.xhtml.

46. Arico, C. et al. Fast Electrochemical Storage Process in Sputtered Nb_2O_5 Porous Thin Films. ACS Nano 13, 5826–5832 (2019).

47. Dash, J. K. et al. A simple growth method for Nb_2O_5 films and their optical properties. RSC Adv 5, 36129–36139 (2015).

48. Guo, W. et al. Enhanced Photocatalytic Activity of Nonuniformly Nitrogen-Doped Nb_2O_5 by Prolonging the Lifetime of Photogenerated Holes. Nanomaterials 12, (2022).

49. Journal of Materials Science: Materials in Electronics 6/2024 | springerprofessional.de. https://www.springerprofessional.de/journal-of-materials-science-materials-in-electronics-6-2024/26762294. (last access 26/03/2025)

50. Guo, Y. et al. Evolution of structure and electrical properties with annealing time in solution-based VO_2 thin films. J Alloys Compd 622, 913–917 (2015).

51. Kalra, M. N. & Kale, B. B. Synthesis of Nitrogen-doped Nb_2O_5 for Energy Application. (2019).

52. Hajakbari, F. & Ensandoust, M. Study of thermal annealing effect on the properties of silver thin films prepared by DC magnetron sputtering. Acta Phys Pol A 129, 680–682 (2016).

53. Luo, Z. et al. Impact of substrate temperature on the microstructure, electrical and optical properties of sputtered nanoparticle V_2O_5 thin films. Vacuum 85, 145–150 (2010).

54. Kim, J. A. et al. Effect of Substrate Temperature on Variations in the Structural and Optical Properties of Cu_2O Thin Films Deposited via RF Magnetron Sputtering. Crystals 2023, Vol. 13, Page 643 13, 643 (2023).

55. Sultana, R., Islam, K. & Chakraborty, S. Tuning Optical and Electrochemical Properties of Nb2O5 Thin Films via WO_3 Doping. Transactions on Electrical and Electronic Materials 26, 48–59 (2024).

56. Dash, J. K. et al. A simple growth method for Nb_2O_5 films and their optical properties. RSC Adv 5, 36129–36139 (2015).

57. Jehng, J. M. & Wachs, I. E. Molecular structures of supported niobium oxide catalysts under ambient conditions. Journal of Molecular Catalysis 67, 369–387 (1991).

58. Lopes, O. F., Paris, E. C. & Ribeiro, C. Synthesis of Nb_2O_5 nanoparticles through the oxidant peroxide method applied to organic pollutant photodegradation: A mechanistic study. Appl Catal B 144, 800–808 (2014).

59. Silva, R. M. et al. Microwave-assisted hydrothermal synthesis and electrochemical characterization of niobium pentoxide/carbon nanotubes composites. J Mater Res 34, 592–599 (2019).

60. Umeshbabu, E. & Ranga Rao, G. High Electrocatalytic Activity of Pt/C Catalyst Promoted by TT-Nb_2O_5 Nanoparticles under Acidic Conditions. ChemistrySelect 2, 4204–4212 (2017).

61. Jehng, J.-M., Turek', A. M. & Wachs, I. E. Surface modified niobium oxide catalyst: synthesis, characterization, and catalysis. Appl Catal A Gen 83, 179–200 (1992).

62. Jehng, J. M. & Wachs, I. E. Structural Chemistry and Raman Spectra of Niobium Oxides. Chemistry of Materials 3, 100–107 (1991).

63. Raman spectra of NiO thin films grown at different sputter powers... | Download Scientific Diagram. https://www.researchgate.net/figure/Raman-spectra-of-NiO-thin-films-grown-at-different-sputter-powers-Inset-after-baseline_fig2_351218803. (last access 26/03/2025)

64. Kim, Y. et al. Phase identification of vanadium oxide thin films prepared by atomic layer deposition using X-ray absorption spectroscopy. RSC Adv 10, 26588–26593 (2020).

65. Sucasaire, W. et al. Raman and infrared spectroscopy studies of carbon nitride films prepared on Si (100) substrates by ion beam assisted deposition. J Braz Chem Soc 17, 1163–1169 (2006).

66. Kulkarni, A. K. et al. Nanostructured N-doped orthorhombic Nb_2O_5 as an efficient stable photocatalyst for hydrogen generation under visible light. Dalton Transactions 46, 14859–14868 (2017).

67. Kalra, M. N. & Kale, B. B. Synthesis of Nitrogen-doped Nb_2O_5 for Energy Application. (2019). Srinivasa Ramanujan Library. Indian Institute of Science Education and Research Pune, India. (2019-03): http://dr.iiserpune.ac.in:8080/xmlui/handle/123456789/4704 (last access 26/03/2025)

68. Lindgren, T. et al. Photoelectrochemical and optical properties of nitrogen doped titanium dioxide films prepared by reactive DC magnetron sputtering. Journal of Physical Chemistry B 107, 5709–5716 (2003).

69. Kreissl, H. T. et al. Structural Studies of Bulk to Nanosize Niobium Oxides with Correlation to Their Acidity. J Am Chem Soc 139, 12670–12680 (2017).

70. Shan, Y. et al. Niobium pentoxide: a promising surface-enhanced Raman scattering active semiconductor substrate. npj Computational Materials 2017 3:1 3, 1–7 (2017).

71. Raba-Páez, A. M., Suarez-Ballesteros, D. N., Martínez-Zambrano, J. J., Rojas-Sarmiento, H. A. & Rincón-Joya, M. Uso del método pechini en la obtención de nanopartículas semiconductoras a base de niobio. DYNA (Colombia) 82, 52–58 (2015).

72. Niederfrequente Raman-Spektroskopie, 410000006-B, 2023-11. https://www.metrohm.com/de_de/applications/bw-tek-applikationen/410000006-b.html (last access 26/03/2025).

73. Liang, X. et al. Fine Control of Optical Properties of Nb_2O_5 Film by Thermal Treatment. Micromachines (Basel) 15, 1453 (2024).

74. Hathal, Y. R., Ibrahim, I. M. & Khalaf, M. K. Effect of Substrate Temperature on Characteristics and Gas Sensing Properties of Nb2O5/Si Thin Films. Iraqi Journal of Applied Physics 20, 271–277 (2024).

75. Mekprasart, W., Khumtong, T., Rattanarak, J., Techitdheera, W. & Pecharapa, W. Selection and peer-review under responsibility of COE of Sustainalble Energy System Effect of Nitrogen Doping on Optical and Photocatalytic Properties of TiO 2 Thin Film Prepared by Spin Coating Process Selection and/or peer-review under responsibility of COE of Sustainable Energy System, Rajamangala University of Technology Thanyaburi(RMUTT). Energy Procedia 34, 746–750 (2013).

76. The characteristics and photocatalytic activity of visible light driven N-doped TiO2. https://www.researchgate.net/publication/289070059_The_characteristics_and_photocatalytic_activity_of_visible_light_driven_N-doped_TiO2.

77. Hu, B. & Liu, Y. Nitrogen-doped Nb2O5 nanobelt quasi-arrays for visible light photocatalysis. J Alloys Compd 635, 1–4 (2015).

78. Moulder, J. F., Stickle, W. F., Sobol, P. E., Bomben, K. D. & Chastain, J. Handbook of X-ray Photoelectron Spectroscopy A Reference Book of Standard Spectra for Identification and Interpretation of XPS Data.

79. High-resolution XPS scan of the O1s region of Nb2O5_550_air. | Download Scientific Diagram. https://www.researchgate.net/figure/High-resolution-XPS-scan-of-the-O1s-region-of-Nb2O5-550-air_fig2_343791273.